İZMİR KÂTİP ÇELEBİ ÜNİVERSİTESİ
2010
GRADUATE SCHOOL OF NATURAL AND APPLIED SCIENCES

Numerical and Experimental Investigation of High Speed Hydrostatic Journal Bearings for Small Gas Turbines

Submitted to the Graduate School of Natural and Applied Sciences
in partial fulfillment of the requirements for the degree of

Master of Science

in Mechanical Engineering

by

Ahmet Yıldırım

ORCID 0009-0001-5042-7921

Advisor: Assoc. Prof. Sercan Acarer

August, 2024

This is to certify that we have read the thesis **Numerical and Experimental Investigation of High Speed Hydrostatic Journal Bearings for Small Gas Turbines** submitted by **Ahmet Yıldırım**, and it has been judged to be successful, in scope and in quality, at the defense exam and accepted by our jury as a MASTER'S THESIS.

APPROVED BY:

Advisor: **Assoc. Prof. Sercan Acarer**
İzmir Kâtip Çelebi University

Committee Members:

Assoc. Prof. Ziya Haktan Karadeniz
İzmir Institute of Technology

Assoc. Prof. Mehmet Akif Ezan
Dokuz Eylül University

Date of Defense: August 26, 2024

Declaration of Authorship

I, **Ahmet Yıldırım**, declare that this thesis titled **Numerical and Experimental Investigation of High Speed Hydrostatic Journal Bearings for Small Gas Turbines** and the work presented in it are my own. I confirm that:

- This work was done wholly or mainly while in candidature for the Master's degree at this university.
- Where any part of this thesis has previously been submitted for a degree or any other qualification at this university or any other institution, this has been clearly stated.
- Where I have consulted the published work of others, this is always clearly attributed.
- Where I have quoted from the work of others, the source is always given. This thesis is entirely my own work, with the exception of such quotations.
- I have acknowledged all major sources of assistance.
- Where the thesis is based on work done by myself jointly with others, I have made clear exactly what was done by others and what I have contributed myself.

Date: 26.08.2024

Numerical and Experimental Investigation of High Speed Hydrostatic Journal Bearings for Small Gas Turbines

Abstract

In recent years, the significance of hybrid journal bearings (combining hydrostatic and hydrodynamic features) has substantially increased in turbomachinery applications. This is due to their capacity for high shaft speeds, heavy load-bearing, and operation across a broad temperature range. Unlike hydrostatic bearings, which use pressurized fluid to separate sliding surfaces, and hydrodynamic bearings, which rely on relative motion and geometry for separation, hybrid bearings leverage the advantages of both types to enhance performance. This study concentrates on the development and analysis of a hybrid bearing manufactured using additive manufacturing techniques, emphasizing self-supported structures. The objective is to investigate a hydrostatic/hydrodynamic bearing capable of handling substantial radial and axial loads and to conduct a numerical analysis of the designed bearing using CFD simulations. Steady-state 3D CFD simulations were conducted to evaluate the bearing's performance. Additionally, a Design of Experiments (DOE) study was conducted, followed by nonlinear regression to create a meta-model predicting the bearing's performance parameters, with results indicating good predictive accuracy. For the experimental component, a journal hydrodynamic bearing test rig was assembled. Experiments were carried out using a cylindrical rotor with a nominal clearance of 300 microns, at various rotational speeds and with two different viscosities. The findings from both numerical and experimental studies provide valuable insights into the performance and feasibility of hybrid bearings in turbomachinery.

Keywords: Hydrostatic Bearing, Hybrid Bearing, Additive Manufacturing, Design of Experiment, Curve Fitting

Küçük Gaz Türbinleri için Yüksek Hızlı Hidrostatik Rulmanların Nümerik ve Deneysel İncelemesi

Öz

Son yıllarda, hibrit mil rulmanlarının (hidrostatik ve hidrodinamik özelliklerin birleşimi) turbomakine uygulamalarında önemi önemli ölçüde artmıştır. Bu, yüksek şaft hızları, ağır yük taşıma kapasitesi ve geniş bir sıcaklık aralığında çalışma yeteneklerinden kaynaklanmaktadır. Hidrostatik rulmanlar, sürtünme yüzeylerini ayırmak için basınçlı sıvı kullanırken, hidrodinamik rulmanlar, ayrımı sağlamak için gövde hareketine ve geometrisine dayanır. Hibrit rulmanlar ise her iki türün avantajlarını birleştirerek performansı artırır. Bu çalışmada, kendinden desteklenen yapıları vurgulayan ve katmanlı üretim teknikleri kullanılarak üretilmiş bir hibrit rulman üzerinde durulmuştur. Amaç, önemli derecede radyal ve eksenel yükleri taşıyabilen bir hidrostatik/hidrodinamik rulmanı araştırmak ve tasarlanan rulmanın performansını HAD simülasyonları kullanarak sayısal olarak analiz etmektir. Sabit durumlu 3D HAD simülasyonları, yatağın performansını değerlendirmek için gerçekleştirilmiştir. Ayrıca, bir Deney Tasarımı (DOE) çalışması yapılmış ve ardından performans parametrelerini tahmin eden bir meta-model oluşturmak için doğrusal olmayan regresyon kullanılmıştır; sonuçlar iyi bir tahmin doğruluğunu göstermektedir. Deneysel bileşen için, bir silindirik rotor ile 300 mikron nominal boşlukta çeşitli dönüş hızlarında ve iki farklı viskozitede yapılan deneylerle bir journal hidrodinamik rulman test donanımı montajlanmıştır. Hem sayısal hem de deneysel çalışmalardan elde edilen bulgular, hibrit rulmanların turbomakine uygulamalarındaki performans ve uygulanabilirliği hakkında değerli bilgiler sağlamaktadır.

Keywords: Hidrostatik Rulman, Hibrit Rulman, Katmanlı Üretim, Deney Tasarımı, Eğri Uydurma

Acknowledgment

This work was supported by NATO Science for Peace and Security (SPS) Programme under Project G5939 titled "Additively Printed Engine" and by the 2023-TYL-FEBE-0018 Project titled "Küçük Gaz Türbin Motorları için Yüksek Hızlı Hidrostatik (Hibrit) Rulmanların Nümerik İncelemesi."

I sincerely thank to the entire Turbomachinery and Heat Transfer Laboratory team for their amazing support and kindness, which have greatly contributed to the success of this study.

I am deeply grateful to Ph.D. Student Michael Palman and Yohai Abraham for their essential assistance in assembling the test rig.

I am deeply appreciative of Assoc. Prof. Beni Çukurel, whose vast expertise and fresh insights have profoundly enhanced the depth and quality of my research.

Finally, I extend my sincere thanks to Assoc. Prof. Sercan Acarer, whose guidance and support from the very beginning have been indispensable throughout this study.

Table of Contents

Declaration of Authorship iii

Abstract iv

Öz v

Acknowledgment vi

List of Figures ix

List of Tables xii

List of Symbols xiii

1 **Introduction** 1

2 **Theory** 5

2.1 Types of Lubrications 5

2.1.1 Hydrodynamic Lubrication 5

2.1.2 Hydrostatic Lubrication 12

2.1.3 Hybrid Lubrication 13

2.2 Types of Fluid Film Bearings 14

2.2.1 Thrust Bearings 14

2.2.2 Journal Bearings 15

2.2.3 Conical Bearings 17

2.3 Computational Fluid Dynamics 18

2.3.1 Turbulence Models 18

2.3.2 Solver Theory 22

2.3.3 Cavitation 23

2.4 Curve Fitting 24

3 **Methodology** 25

4 **Results** 37

4.1 Entire Bearing Geometry Overview 37

4.2 Design of Experiment (DoE) 41

4.3 A Hydrodynamic Bearing Test Rig 49

5 **Conclusion** 51

References 52

List of Figures

Figure 2.1 The principle of hydrodynamic lubrication [25]. 5

Figure 2.2 The equilibrium of a fluid element within a hydrodynamic film [25].....6

Figure 2.3 Velocity distributions at the entrance of the hydrodynamic film [25].....8

Figure 2.4 Flow continuity in a column [25] 9

Figure 2.5 A represantation of hydrostatic lubrication 13

Figure 2.6 Common thrust bearings [25] 14

Figure 2.7 Representation of a journal bearing geometry [25] 15

Figure 2.8 Full-sommerfeld and half-sommerfeld conditions [25].....16

Figure 2.9 Recessed and plain conical bearing [27] 17

Figure 2.10 Pressure-based solution methods [28] 22

Figure 2.11 Density-based solution method [28].....23

Figure 3.1 A representation of a four-pocket hybrid journal bearing 25

Figure 3.2 The entire hybrid bearing geometry 27

Figure 3.3 A mesh structure of the hybrid bearing geometry 27

Figure 3.4 A single cone bearing geometry [27].....28

Figure 3.5 A bearing test rig 33

Figure 3.6 The bearing test rig 33

Figure 3.7 A LabVIEW code for pressure and temperature measurement 35

Figure 3.8 The hydrodynamic journal bearing test rig.....36

Figure 4.1 Cavitation areas 37

Figure 4.2 Wall shear stresses.....38

Figure 4.3 Pressure distributions.....38

Figure 4.4 Bearing's fluid velocity field.....39

Figure 4.5 Comparison of load carrying capacity per shaft area 40

Figure 4.6 Comparison of friction losses per shaft area.....40

Figure 4.7 Mesh sensitivity analysis 41

Figure 4.8 Represantation of cavitation zones by vapor volume fraction.....42

Figure 4.9 Skin friction on the shaft surface 42

Figure 4.10 Velocity vectors of the lubricant.....43

Figure 4.11 Pi groups and flow coefficient.....44

Figure 4.12 Pi groups and friction coefficient 44

Figure 4.13 Pi groups and axial load coefficient.....45

Figure 4.14 Pi groups and radial load coefficient 45

Figure 4.15 Predicted and observed flow coefficients from meta-model and CFD.....47

Figure 4.16 Predicted and observed friction coefficients from meta-model and CFD 47

Figure 4.17 Predicted and observed axial load capacity coefficients from meta-model and CFD 48

Figure 4.18 Predicted and observed radial load capacity coefficients from meta-model and CFD 48

Figure 4.19 Boundary conditions.....49

Figure 4.20 Pressure distribution of the water lubricated bearing at 4000 rpm.....50

Figure 4.21 A comparison of static pressures at various rotational speed.....50

List of Tables

Table 3-1 A result of verification study 26

Table 3-2 Ansys FLUENT setup 28

Table 3-3 Levels of pi groups 31

Table 3-4 Taguchi's L27 orthogonal array 32

List of Symbols

α	Semi cone angle
Γ_k, Γ_ω	The effective diffusivity of k and ω
η	Kinematic viscosity [m^2/s]
ε	Rate of dissipation of turbulent kinetic energy [m^2/s^3]
θ	Circumferential coordinate
μ	Dynamic viscosity [Pa.s]
μ_m	The viscosity of mixture [Pa.s]
ρ	Density of the lubricant [kg/m^3]
ρ_m	Mixture density [kg/m^3]
σ_ε	Thee turbulent Prandtl number for rate of dissipation of turbulent kinetic energy
σ_k	The turbulent Prandtl number for turbulent kinetic energy
$\sigma_{\tilde{\eta}}$	Constant in spalart allmaras model
τ	Shear stress [Pa]
τ_x	Shear stress in x direction [Pa]

τ_y	Shear stress in x direction [Pa]
ω	Specific rate of dissipation [1/s]
a	Axial bearing land width [m]
B	Width of the bearing [m]
c	Nominal clearance [m]
$C_{1\varepsilon}$, $C_{2\varepsilon}$,$C_{3\varepsilon}$	Constants in k-ε model
C_{b2}	Constant in Spalart-Allmaras model
D	Diameter of the bearing [m]
e	Eccentricity [m]
F	Friction loss [W]
$\vec{F}$	Body force
$\bar{f}$	Coefficient of friction based on relationship between the load and friction loss
G_η	The production of turbulent viscosity
G_ω	The generation of specific rate of dissipation
G_b	The generation of turbulence kinetic energy due to buoyancy
G_k	The generation of turbulence kinetic energy due to the mean velocity gradients

k	Turbulent kinetic energy [m^2/s^2]
L	Length of the bearing [m]
p	Pressure [Pa]
ΔP	Total-to-static pressure difference [Pa]
q_x, q_y	Flow rates per unit length and unit width
Q	Volume flow rate [m^3/s]
$\overline{Q}$	Flow coefficient
Q_x, Q_y	The lubricant leakage
R, r	Radius of a bearing [m]
S_ε, S_k	User defined source terms in k-ε model
S_ϕ	Source term of ϕ per unit volume
S_ω, S_k	User defined source terms in k-ω model
$S_{\tilde{\eta}}$	User defined source term in Spallart-Allmaras model
u	The sliding velocity in the 'x' direction [m/s]
U	Tangential speed at the mean radius [m/s]
v	The sliding velocity in the 'y' direction [m/s]
$\overrightarrow{v_m}$	The mass-averaged velocity [m/s]

$\overrightarrow{v_{dr,k}}$	The drift velocity for secondary phase k [m/s]
W	Load capacity [N]
W_A	Axial load capacity [N]
$\overline{W_A}$	Axial load coefficient
W_R	Radial load capacity [N]
$\overline{W_R}$	Radial load coefficient
w_0	The velocity at which the bottom of the column moves up
w_h	The velocity at which the top of the column moves up
x	x direction [m]
y	y direction [m]
Y_η	The destruction of turbulent viscosity
Y_k, Y_ω	The dissipation of k and ω due to turbulence
Y_M	The contribution of the fluctuating dilatation in compressible turbulence to the overall dissipation rate
z	z direction [m]

Chapter 1

Introduction

Having a capability to carry radial and axial loads, hydrostatic and hydrodynamic bearings have been used in many applications such as turbomachinery, aerospace and industrial machinery. The increasing need for advanced bearing technologies, from small precision tools to large equipment, has led researchers to study hydrostatic and hydrodynamic bearings for a long time [1][2].

A hydrostatic bearing is a type of fluid bearing that carries load with a continuous supply of pressurized fluid to create a thin film between a stationary bearing surface and moving surfaces. Hydrostatic bearings need an outside pressure source to function properly. The external supply system pumps pressurized lubricant into the bearing clearance, the pressure of the lubricant creates a fluid film that separates the stationary and moving surfaces and the pressurized lubricant film can support loads. Hooke and et.al.[3] presented a way to optimize the design of the multi-recess, externally pressurized bearing for optimal power efficiency, minimal leakage, and maximum stiffness, by using an operating parameter. Nypan and et.al. [4] analyzed a conical hydrostatic bearing to minimize friction, developing equations for optimal bearing configurations that results in the lowest friction torque under both laminar and turbulent flow conditions and it was seen that while hydrostatic pocket friction significantly impacts friction torque, its effect on pocket friction itself is minimal. L. San Andres et al. [5] introduced a bulk-flow thermodynamic analysis to determine performances characteristics for turbulent flow, comparing numerical predictions of flow and rotor dynamic force coefficients with experimental results from a water-lubricated hydrostatic bearing. Sharma and et.al.[6] conducted a theoretical analysis of a 4-pocket hydrostatic conical journal bearing,

focusing on performance by solving the Reynolds equation. Li and et. al.[7] created a mathematical model for angled-surface slot-compensated hydrostatic bearing (ASHB) and solved this model by Finite Element Method (FEM). Results are compared with the traditional fixed slot-compensated hydrostatic bearings and it is shown that the performance of ASHB is better than the performance of fixed slot-compensated hydrostatic bearing (FSHB). Wang and et.al.[8] developed a novel approach to calculate the bearing capacity of a four-rectangle recessed hydrostatic journal bearing, considering various operating conditions and structural parameters in their numerical analysis.

Different from hydrostatic bearings, hydrodynamic bearings rely on the relative motion between surfaces to provide the necessary lubrication. Hydrodynamic bearings operate on the principle of hydrodynamic lubrication. When a moving surface begins to move, it pulls the viscous fluid into the convergent wedge, generating pressure in the lubricant that carries the applied load. This thin or thick lubricant film separates the stationary and moving surfaces and prevents direct metal-to-metal contact. Raimondi and Boyd[2][9][10] developed a method to calculate the performance parameters of the journal bearing utilizing the relationships between Sommerfeld number and minimum film-thickness, the temperature-rise variable, the friction variable, the flow ratio, and the attitude angle. Manser and et.al.[11] analyzed how bearing surface texturing and journal misalignment affect hydrodynamic journal bearing performance using a numerical model incorporating the Elrod-Adams mass-conserving cavitation algorithm with the Reynolds equation. Feng and et.al.[12] developed a model to predict the performance of water-lubricated hydrodynamic journal bearings under misalignment, accounting for turbulent flow. They found that both thermodynamic and turbulent effects significantly influence dynamic coefficients in both aligned and misaligned states. Milčić and et.al.[13] utilized an artificial neural network (ANN) to predict the friction coefficient of a hydrodynamic journal bearing in their study. Experimental data for their research were obtained by testing the journal bearing that is suitable for hydrodynamic lubrication. The study demonstrated that using ANN for predicting the friction coefficient is an effective approach. Ma and et.al. [14] examined the effects of angular misalignment on the lubrication performance of cylindrical hydrodynamic journal bearings, focusing on stochastic behavior. Zhang and et.al. [15] developed a model for high-speed water-

lubricated journal bearings that incorporates cavitation effects and verified it experimentally. Dong and et.al. [16] introduced a new method to calculate hydrostatic journal bearing performance, which proved to be more efficient, precise, and stable than traditional methods such as FDM and Liang's approach.

In essence, a hydrostatic bearing uses external pressurization to create a lubricating film between bearing surfaces to support a load on a bearing. On the other hand, a hydrodynamic bearing relies on relative motion to generate a lubricant film. The motion itself creates a pressure within the lubricant that lifts and supports the load. Hybrid bearings combine these two principles of external pressurization and high speed, allowing them to operate at zero or very low speed as well as high speeds, thereby increasing their load capacity. Stout and Rowe [1][17] , provided designers with information and guidance for designing both gas and liquid feed bearings. This study includes selection of bearing configuration, manufacturing technique, material and control devices. Rowe [18] investigated three-recess and four-recess conical bearings at high-speed combining hydrostatic and hydrodynamic load supports. It is shown that long and narrow recess bearings provide better hybrid load performance compared with wide-recess bearings. Hong and et.al. [19] performed both theoretical and experimental investigations on externally pressurized deep/shallow pocket hybrid conical bearings to assess dynamic performance. Their study revealed that hybrid conical bearings provide superior load capacity and stability compared to conventional hydrostatic and hydrodynamic bearings, as corroborated by their numerical and experimental data. Heller and Shapiro [20] developed a numerical method to evaluate the performance of hybrid journal bearings, accounting for various clearance distributions and cavitation effects by solving the incompressible Reynolds equation. Dumbrava [21] devised a comprehensive mathematical model to assess the hydrostatic contributions to bearing performance, offering valuable insights for optimizing hybrid bearing design. Kennedy and et.al. [22][23] examined the theoretical and experimental behavior of externally pressurized central recess conical bearings. Their study assumed isothermal laminar flow for a viscous incompressible fluid, taking into account nonuniform film thickness. Guo [24] modeled a hybrid journal bearing for two scenarios: one with constant fluid properties and another with temperature-dependent fluid properties, which provided a more realistic simulation.

With temperature-dependent properties, the maximum pressure, attitude angle, load capacity, and flow rate decreased compared to constant properties. Despite this, the hybrid bearing still exhibited higher load capacity and pressure field than both hydrostatic and hydrodynamic bearings.

The purpose of this research is to investigate journal and conical hybrid bearings used in high-speed small gas turbines, both numerically and experimentally. The final hybrid bearing design will be manufactured using additive manufacturing techniques, which introduces certain design constraints. The bearing design is expected to have a nominal clearance of approximately 300 microns, a value not commonly found in existing literature. Consequently, current literature cannot serve as a design guideline completely. Therefore, each dimensionless parameter of the bearing will be examined individually. Additionally, the design has to be self-supporting to minimize post-processing and allow for printing rotating surfaces embedded within the stator. Upon completion, this study will serve as a guideline for designers working with larger nominal clearances and additive manufacturing technologies.

Chapter 2

Theory

2.1 Types of Lubrications

There are various types of lubrications described in the literature but this study focuses on only two types of fluid film lubrication: hydrodynamic lubrication and hydrostatic lubrication.

2.1.1 Hydrodynamic Lubrication

Hydrodynamic lubrication relies on the relative motion between stationary and moving surfaces to generate pressure in the lubricant to support the load. Hydrodynamic lubrication happens when the lubricant layer is thick enough to completely separate moving and stationary surfaces, preventing contact. As the surfaces slide past one another, the lubricant is drawn into gap between them, creating a pressure buildup that forms a film. The principle of hydrodynamic lubrication is shown in Figure 2.1.

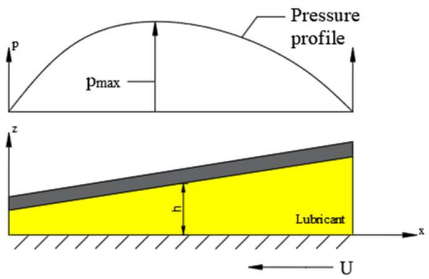

Figure 2.1: The principle of hydrodynamic lubrication [25].

Reynolds [26] was the first to analytically demonstrate that a viscous liquid can physically separate two sliding surfaces through hydrodynamic pressure. All forms of hydrodynamic lubrication can be mathematically represented by an equation derived by Reynolds. Though derived from the Navier-Stokes equations, it is typically obtained by examining the equilibrium of a liquid element under viscous shear and ensuring continuity of flow.

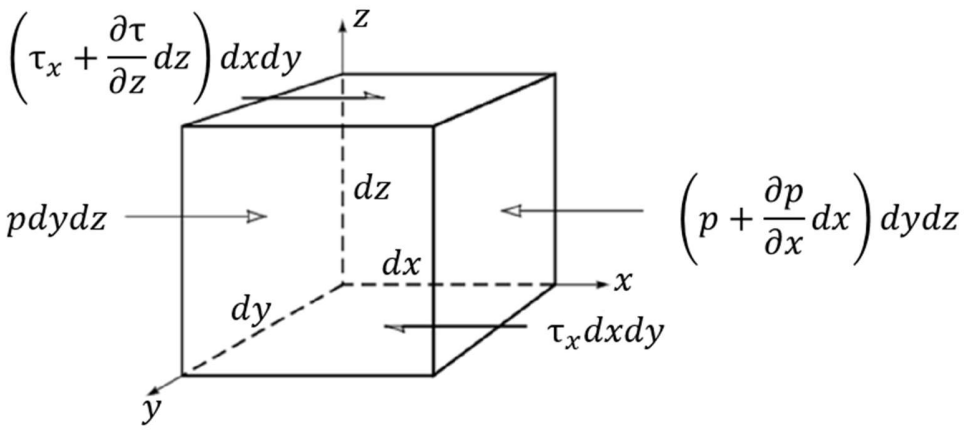

Figure 2.2: The equilibrium of a fluid element within a hydrodynamic film [25]

Consider a small fluid element within a hydrodynamic film depicted in Figure 2.2, with forces acting only in the 'x' direction. In equilibrium, the forces on the left side balance the forces on the right side, so

$$pdydz + \left(\tau_x + \frac{\partial \tau_x}{\partial z} dz\right) dxdy = \left(p + \frac{\partial p}{\partial x} dx\right) dydz + \tau_x dxdy \tag{2.1}$$

which simplifies to

$$\frac{\partial \tau_x}{\partial z} dxdydz = \frac{\partial p}{\partial x} dxdydz \tag{2.2}$$

It is non zero volume, so $dxdydz \neq 0$ and both sides can be divided by this value,

$$\frac{\partial \tau_x}{\partial z} = \frac{\partial p}{\partial x} \tag{2.3}$$

For 'y' direction, this can be written,

$$\frac{\partial \tau_y}{\partial z} = \frac{\partial p}{\partial y} \tag{2.4}$$

In ‘z’ direction, there is no pressure gradient,

$$\frac{\partial p}{\partial x} = 0 \tag{2.5}$$

Shear stresses in the 'x' and 'y' directions can be formulated based on dynamic viscosity and shear rates as follows:

$$\tau_x = \frac{u}{h} = \mu \frac{\partial u}{\partial z} \tag{2.6}$$

$$\tau_y = \frac{v}{h} = \mu \frac{\partial v}{\partial z} \tag{2.7}$$

Applying Equation (2.6) into Equation (2.3) and Equation (2.7) into Equation (2.4), the forces acting in the ‘x’ and ‘y’ directions are determined:

$$\frac{\partial p}{\partial x} = \frac{\partial}{\partial z}\left(\mu \frac{\partial u}{\partial z}\right) \tag{2.8}$$

$$\frac{\partial p}{\partial y} = \frac{\partial}{\partial z}\left(\mu \frac{\partial v}{\partial z}\right) \tag{2.9}$$

Equation (2.8) and (2.9) can be integrated, assuming the fluid’s viscosity is constant throughout the film and independent of ‘z’.

$$\frac{\partial p}{\partial x} dz = \mu \frac{\partial^2 u}{\partial z^2}$$

$$\frac{\partial p}{\partial x} z + C_1 = \mu \frac{\partial u}{\partial z}$$

$$\left(\frac{\partial p}{\partial x} z + C_1\right) dz = \mu du$$

$$\frac{\partial p}{\partial x} \frac{z^2}{2} + C_1 z + C_2 = \mu u \tag{2.10}$$

There is no slip, so the boundary conditions are:

$u = U_2$ at $z = 0$

$u = U_1$ at $z = h$

The constants 'C_1' and 'C_2' are:

$$C_1 = (U_1 - U_2)\frac{\mu}{h} - \frac{\partial p}{\partial x}\frac{h}{2}$$

$$C_2 = \mu U_2$$

$$\frac{\partial p}{\partial x}\frac{z^2}{2} + (U_1 - U_2)\frac{\mu z}{h} - \frac{\partial p}{\partial x}\frac{hz}{2} + \mu U_2 = \mu u$$

After simplification, the velocity in the 'x' direction and 'y' directions can be expressed as:

$$u = \left(\frac{z^2 - zh}{2\mu}\right)\frac{\partial p}{\partial x} + (U_1 - U_2)\frac{z}{h} + U_2 \qquad (2.11)$$

$$v = \left(\frac{z^2 - zh}{2\mu}\right)\frac{\partial p}{\partial y} + (U_1 - U_2)\frac{z}{h} + V_2 \qquad (2.12)$$

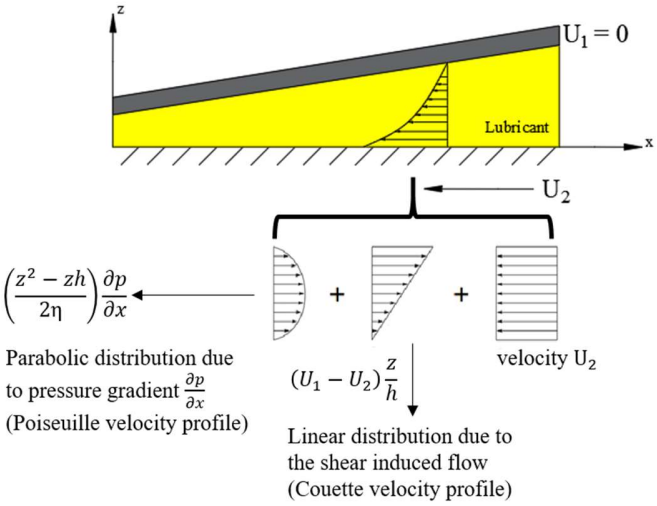

Figure 2.3: Velocity distributions at the entrance of the hydrodynamic film [25]

The three individual terms in velocity, Equation (2.11) and Equation (2.12) represent the flow velocities within the fluid film, as illustrated in Figure 2.3.

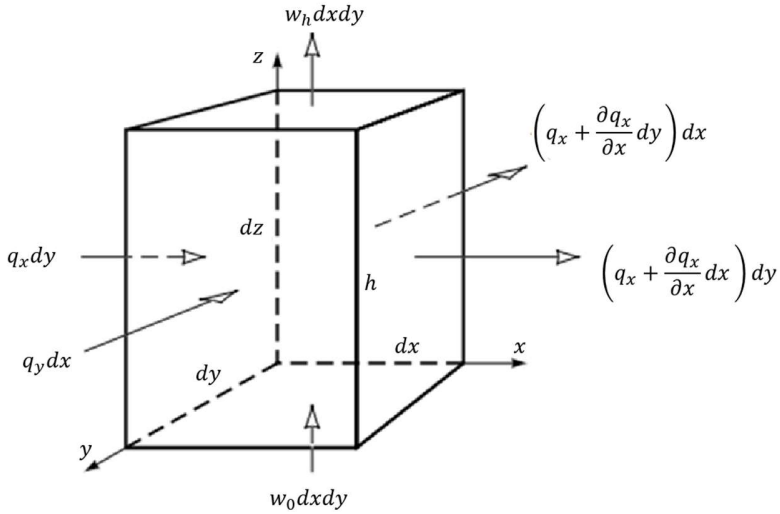

Figure 2.4: Flow continuity in a column [25]

Imagine a fluid flow depicted in Figure 2.4, according to the continuity of flow principle, under steady-state conditions, the volume of liquid entering must equal the volume exiting a control region The lubricant enters the column horizontally at rates of $q_x$and q_y and leaves the column at rates of $q_x + \frac{\partial q_z}{\partial x} dx$ and $q_y + \frac{\partial q_z}{\partial y} dy$ per unit length and width. In the vertical direction, the lubricant enters the column at a rate of $w_0 dxdy$ and exits the column at a rate of $w_h dxdy$ with different velocities. If the lubricant density remains constant, we can write this:

$$q_x dy + q_y dx + w_0 dxdy = \left(q_x + \frac{\partial q_x}{\partial x} dx\right) dy + \left(q_y + \frac{\partial q_y}{\partial y} dy\right) dx + w_h dxdy \tag{2.13}$$

after simplifying:

$$\frac{\partial q_x}{\partial x} dxdy + \frac{\partial q_y}{\partial y} dxdy + (w_h - w_0) dxdy = 0 \tag{2.14}$$

$dxdy \neq 0$ so, we can rewrite the Equation (2.14) as:

$$\frac{\partial q_x}{\partial x} + \frac{\partial q_y}{\partial y} + (w_h - w_0) = 0 \tag{2.15}$$

q_x and q_y,are derived by integrating the velocity profile of the lubricant throughout the film thickness:

$$q_x = \int_0^h u dz \tag{2.16}$$

$$q_y = \int_0^h v dz \tag{2.17}$$

By substituting 'u' and 'y' from Equation (2.11) and Equation (2.12), we can determine the flow rates in 'x' and 'y' directions:

$$q_x = -\frac{h^3}{12\mu}\frac{\partial p}{\partial x} + (U_1 + U_2)\frac{h}{2} \tag{2.18}$$

$$q_y = -\frac{h^3}{12\mu}\frac{\partial p}{\partial y} + (V_1 + V_2)\frac{h}{2} \tag{2.19}$$

Now, substituting (2.18) and (2.19) into Equation (2.15):

$$-\frac{\partial}{\partial x}\left[-\frac{h^3}{12\mu}\frac{\partial p}{\partial x} + (U_1 + U_2)\frac{h}{2}\right] + \frac{\partial}{\partial y}\left[-\frac{h^3}{12\mu}\frac{\partial p}{\partial y} + (V_1 + V_2)\frac{h}{2}\right] + (w_h - w_0) = 0 \tag{2.20}$$

Let $U = U_1 + U_2$ and V= $V_1 + V_2$, we can obtain the complete Reynolds equation in three dimensions:

$$\frac{\partial}{\partial x}\left(\frac{h^3}{\mu}\frac{\partial p}{\partial x}\right)+\frac{\partial}{\partial y}\left(\frac{h^3}{\mu}\frac{\partial p}{\partial y}\right)=6\left(U\frac{\partial h}{\partial x}+V\frac{\partial h}{\partial y}\right)+12(w_h-w_0) \tag{2.21}$$

The full form of the Reynolds equation is often intricate for practical engineering applications and most studies generally apply these simplifications:

For example, in a journal bearing we can assume that one of the velocities is zero, $V = 0$, and delete this term from Equation (2.21):

$$\frac{\partial}{\partial x}\left(\frac{h^3}{\mu}\frac{\partial p}{\partial x}\right)+\frac{\partial}{\partial y}\left(\frac{h^3}{\mu}\frac{\partial p}{\partial y}\right)=6\left(U\frac{\partial h}{\partial x}\right)+12(w_h-w_0) \tag{2.22}$$

In addition, it can be assumed that vertical flow through the film is absent and can rewrite Equation (2.22):

$$\frac{\partial}{\partial x}\left(\frac{h^3}{\mu}\frac{\partial p}{\partial x}\right)+\frac{\partial}{\partial y}\left(\frac{h^3}{\mu}\frac{\partial p}{\partial y}\right)=6\left(U\frac{\partial h}{\partial x}\right) \tag{2.23}$$

Disregarding thermal effects in hydrodynamic films implies that the lubricant viscosity stays uniform across the film:

$$\frac{\partial}{\partial x}\left(h^3\frac{\partial p}{\partial x}\right)+\frac{\partial}{\partial y}\left(h^3\frac{\partial p}{\partial y}\right)=6U\mu\frac{\partial h}{\partial x} \tag{2.24}$$

By using the Reynolds equation, it is possible to derive several critical design parameters for bearings, including pressure distribution, load capacity, friction loss, coefficient of friction, and lubricant flow. These parameters can be obtained through straightforward integration techniques, providing essential insights into the bearing's performance characteristics. The pressure distribution within a hydrodynamic lubricating film is found by integrating the Reynolds equation over a defined film shape, $h = f(x, y)$. Integrating this pressure over the bearing area allows for the calculation of the load capacity. The load capacity for a bearing with a particular film geometry is:

$$W = \int_0^L \int_0^B p dx dy \tag{2.25}$$

Assuming friction is only due to fluid shearing, the total friction force in the hydrodynamic film can be obtained by integrating the shear stress 'τ' across the entire bearing surface:

$$F = \int_0^L \int_0^B \tau dx dy \tag{2.26}$$

The shear stress 'τ' is:

$$\tau = \mu \frac{\partial u}{\partial z}$$

The relationship between the load and friction forces gives the coefficient of the friction:

$$\bar{f} = \frac{F}{W} = \frac{\int_0^L \int_0^B \tau dx dy}{\int_0^L \int_0^B p dx dy} \tag{2.27}$$

Integrating 'q_x' and 'q_y' (2.18) and (2.19) determines the lubricant leakage:

$$\begin{aligned} Q_x &= \int_0^L q_x dy \\ Q_y &= \int_0^L q_y dx \end{aligned} \tag{2.28}$$

2.1.2 Hydrostatic Lubrication

In this type of lubrication, the bearing surfaces are completely separated by a lubricating layer composed of liquid or gas, which is actively pushed between the surfaces by an external pump-generated pressure. This contrasts with hydrodynamic lubrication, where the pressure primarily arises from viscous drag within the lubricant. In hydrostatic systems, the external pump applies pressure to maintain the separation, ensuring smooth

operation and reduced friction between the bearing surfaces. Figure 2.5 illustrates a representation of hydrostatic lubrication.

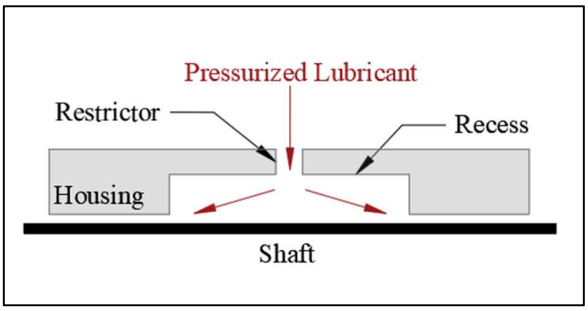

Figure 2.5: A represantation of hydrostatic lubrication

Hydrostatic bearings necessitate flow control mechanisms to regulate film pressures, ensuring they adjust according to applied loads. Hydrostatic bearings require flow control mechanisms to precisely regulate film pressures in response to applied loads. Some examples of flow control devices types are laminar or turbulent restrictors and constant flow or pressure-sensing valves. Capillary tubes or restrictors have small diameters, which create a pressure drop. In orifice restriction system, a small orifice is installed in the lubricant supply line. This orifice restricts fluid flow, inducing a pressure drop that ensures the lubricant is delivered to the gap at the desired pressure. Constant-flow control typically involves maintaining a steady flow rate of lubricant to ensure a consistent film thickness between the bearing surfaces. There are two main types of pressure-sensing valves: spool valves and diaphragm valves. These valves play a crucial role in adjusting flow restrictions based on the load applied to the bearing. An ideal pressure-sensing valve increases the flow rate proportionally to the bearing load. This capability ensures a consistent film thickness, operating within the system's linear limits.

2.1.3 Hybrid Lubrication

Hybrid lubrication is a lubrication system that integrates different lubrication mechanisms to achieve optimal performance, especially in demanding applications. Typically, it combines hydrodynamic and hydrostatic lubrication principles. This dual mechanism

ensures effective lubrication and enhances the bearing's performance under various operating conditions.

2.2 Types of Fluid Film Bearings

Fluid bearings, which utilize a thin layer of fluid to support loads and minimize friction, are essential components in many mechanical systems. These bearings function by maintaining a fluid layer between the moving surfaces. There are several primary types of fluid bearings, each serving different applications and requirements. Here are some of the main types:

2.2.1 Thrust Bearings

These bearings are specifically engineered to carry axial loads, which are loads that act oriented along the axis of rotation. They are commonly used in applications where the primary load is in the axial direction, such as in turbines and propellers. Some examples are depicted in Figure 2.6.

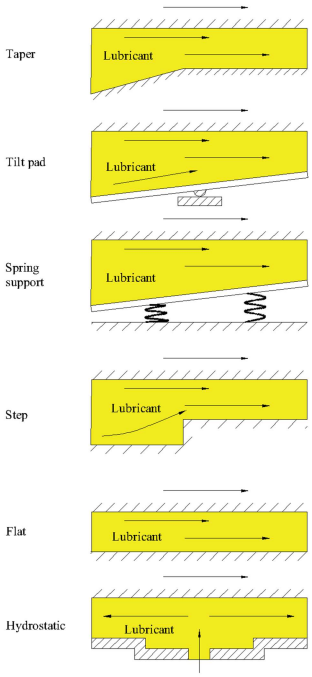

Figure 2.6: Common thrust bearings [25]

The behavior of the lubricant follows the fundamental hydrodynamic principles applicable to journal bearings. The Reynolds equation, initially developed in cartesian coordinates, is expressed as follows when converted to cylindrical coordinates:

$$\frac{\partial}{\partial r}\left(\frac{\rho r h^3}{12\mu}\frac{\partial p}{\partial r}\right)+\frac{1}{r}\frac{\partial}{\partial \theta}\left(\frac{h^3}{12\mu}\frac{\partial p}{\partial \theta}\right)=U\left(\frac{\partial (ph)}{\partial x}\right)-12r\rho V_s \tag{2.29}$$

2.2.2 Journal Bearings

Journal bearings comprise a housing surrounding a rotor, designed to carry a radial load. It features a stationary bushing that may have a complete 360° arc or various configurations of partial arcs within a housing structure.

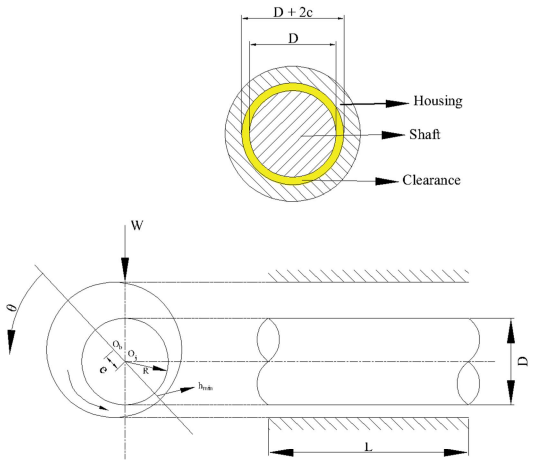

Figure 2.7: Representation of a journal bearing geometry [25]

The design of a cylindrical bearing is illustrated in Figure 2.7. Its circumferential coordinate, denoted as θ, which corresponds to the point of maximum film thickness. The film thickness, h, is given by the following approximation:

$$h = c + e\cos\theta \tag{2.30}$$

where c is the nominal clearance.

In the analysis, the Full-Sommerfeld boundary condition I often used. The Full-Sommerfeld boundary condition assumes that the pressure in the lubricant film is continuous around the entire bearing, including at the film rupture point (where the film cavitates). This condition often leads to the prediction of negative pressures in some regions of the film. While real fluids can cavitate and form vapor cavities at negative pressures, this classical boundary condition does not account for cavitation explicitly. The Full-Sommerfeld boundary condition is useful for theoretical analyses and provides a continuous solution for the pressure distribution. However, it does not accurately model cavitation phenomena, which leads to the formation of vapor cavities. Compared to the Full-Sommerfeld boundary condition, which assumes pressure continuity without explicit consideration of cavitation, the Half-Sommerfeld condition offers a more realistic representation of the physical phenomenon. Pressure distributions are shown in Figure 2.8

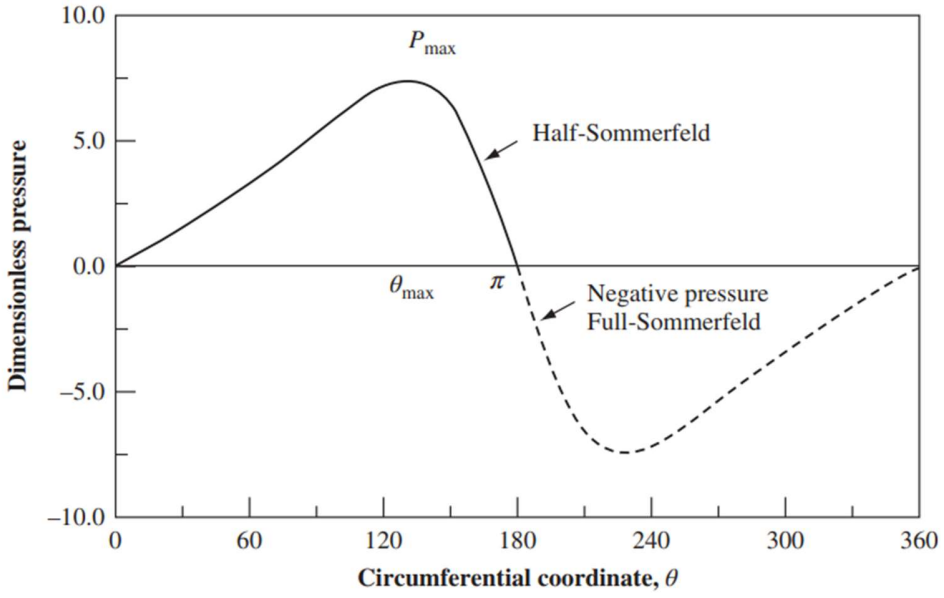

Figure 2.8: Full-sommerfeld and half-sommerfeld conditions [25]

2.2.3 Conical Bearings

The bearing features a conical shape, which offers enhanced load distribution compared to traditional cylindrical bearings. This conical geometry improves the bearing's ability to manage both radial and axial forces. Additionally, these bearings possess the capability for both hydrodynamic and hydrostatic operation, providing versatile performance characteristics. Consequently, conical bearings are widely utilized in applications such as turbomachinery, high-precision machine tools, and spindles, where efficient load handling and reliability are crucial. A recessed bearing is contrasted with a plain bearing in Figure 2.9. Bearings with five or six recesses exhibit slightly superior load-bearing and stiffness performance compared to those with four recesses. In contrast, plain slot-entry bearings typically feature two rows of 12 slots each. While these slot-entry bearings offer better load performance than four-recess bearings, they tend to generate slightly more friction drag. Each recess is supplied with a constant gauge supply pressure Ps through an individual flow control device. A capillary or slot restrictor is required for each recess or slot entry to regulate the flow.

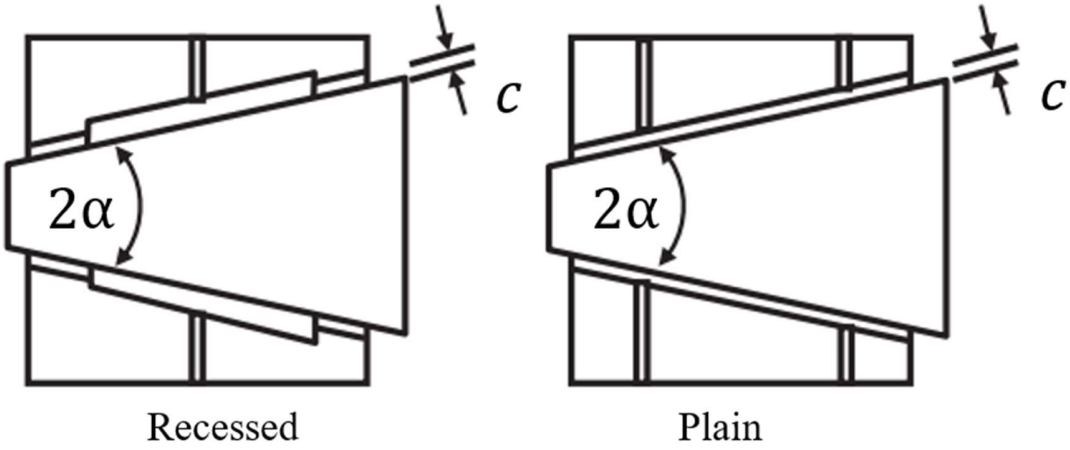

Figure 2.9: Recessed and plain conical bearing [27]

2.3 Computational Fluid Dynamics

Conducting CFD simulations for conical hydrostatic/hydrodynamic bearings is essential to understand the fluid flow and pressure distribution within the bearing clearance. These simulations enable the optimization of design parameters, prediction of performance characteristics like load capacity and friction, and identification of potential issues such as cavitation. By providing detailed insights without the need for extensive physical testing, CFD simulations help improve the efficiency, reliability, and lifespan of the bearings while reducing development costs.

2.3.1 Turbulence Models

Turbulent flows feature fluctuating velocity fields that mix momentum, energy, and species concentration, causing these quantities to fluctuate. Directly simulating these small-scale, high-frequency fluctuations is computationally intensive. Engineers instead use time-averaging, ensemble-averaging, or other methods to simplify the equations, making them computationally feasible. However, this introduces additional unknowns, requiring turbulence models to resolve. These models estimate the unknowns from known quantities, enabling accurate turbulent flow simulations. Common turbulence models include:

2.3.1.1 Reynolds-Averaged Navier-Stokes Models

The Reynolds-averaged Navier-Stokes (RANS) equations govern the transport of averaged flow quantities, modeling the entire range of turbulence scales.

- **Spalart-Allmaras model**

The Spalart-Allmaras model is a straightforward one-equation model that addresses the transport equation for kinematic eddy (turbulent) viscosity. The transport equation for Spalart-Allmaras model is:

$$\frac{\partial}{\partial t}(\rho\tilde{\eta}) + \frac{\partial}{\partial x_i}(\rho\tilde{\eta}u_i) = G_\eta + \frac{1}{\sigma_{\tilde{\eta}}}\left[\frac{\partial}{\partial x_j}\left\{(\mu + \rho\tilde{\eta})\frac{\partial\tilde{\eta}}{\partial x_j}\right\} + C_{b2}\rho\left(\frac{\partial\tilde{\eta}}{\partial x_j}\right)^2\right] - Y_\eta + S_{\tilde{\eta}} \quad (2.31)$$

- **k-ε models**

The k-ε (k-epsilon) turbulence models are extensively utilized in computational fluid dynamics (CFD) to simulate turbulent effects. These are two-equation models that solve transport equations for turbulent kinetic energy (k) and its dissipation rate (ε). Various versions of the k-ε model exist, each tailored to different formulations and applications. The three most commonly used variants are the Standard k-ε, RNG k-ε, and Realizable k-ε models. The turbulence kinetic energy, k, and its rate of dissipation, ε, are obtained from the following transport equations for standard k-ε model:

$$\frac{\partial}{\partial t}(\rho k) + \frac{\partial}{\partial x_i}(\rho k u_i) = \frac{\partial}{\partial x_j}\left[\left(\mu + \frac{\mu_t}{\sigma_k}\right)\frac{\partial k}{\partial x_j}\right] + G_k + G_b - \rho\varepsilon - Y_M + S_k \quad (2.32)$$

and

$$\frac{\partial}{\partial t}(\rho\varepsilon) + \frac{\partial}{\partial x_i}(\rho\varepsilon u_i) = \frac{\partial}{\partial x_j}\left[\left(\mu + \frac{\mu_t}{\sigma_\varepsilon}\right)\frac{\partial\varepsilon}{\partial x_j}\right] + C_{1\varepsilon}\frac{\varepsilon}{k}(G_k + C_{3\varepsilon}G_b) - C_{2\varepsilon}\rho\frac{\varepsilon^2}{k} + S_\varepsilon \quad (2.33)$$

The RNG k-ε model:

$$\frac{\partial}{\partial t}(\rho k) + \frac{\partial}{\partial x_i}(\rho k u_i) = \frac{\partial}{\partial x_j}\left[\alpha_k \mu_{eff} \frac{\partial k}{\partial x_j}\right] + G_k + G_b - \rho\varepsilon - Y_M + S_k \tag{2.34}$$

and

$$\frac{\partial}{\partial t}(\rho\varepsilon) + \frac{\partial}{\partial x_i}(\rho\varepsilon u_i) = \frac{\partial}{\partial x_j}\left[\alpha_\varepsilon \mu_{eff} \frac{\partial \varepsilon}{\partial x_j}\right] + C_{1\varepsilon}\frac{\varepsilon}{k}(G_k + C_{3\varepsilon}G_b) - C_{2\varepsilon}\rho\frac{\varepsilon^2}{k} - R_\varepsilon + S_\varepsilon \tag{2.35}$$

The realizable k-ϵ model is:

$$\frac{\partial}{\partial t}(\rho k) + \frac{\partial}{\partial x_j}(\rho k u_j) = \frac{\partial}{\partial x_j}\left[\left(\mu + \frac{\mu_t}{\sigma_k}\right)\frac{\partial k}{\partial x_j}\right] + G_k + G_b - \rho\varepsilon - Y_M + S_k \tag{2.36}$$

and

$$\frac{\partial}{\partial t}(\rho\varepsilon) + \frac{\partial}{\partial x_j}(\rho\varepsilon u_j) = \frac{\partial}{\partial x_j}\left[\left(\mu + \frac{\mu_t}{\sigma_\varepsilon}\right)\frac{\partial k}{\partial x_j}\right] + \rho C_{1\varepsilon} S_\varepsilon - \rho C_2 \frac{\varepsilon^2}{k + \sqrt{v\varepsilon}} + C_{1\varepsilon}\frac{\varepsilon}{k} C_{3\varepsilon} G_b + S_\varepsilon \tag{2.37}$$

where

$$C_{1\varepsilon} = max\left[0.43, \frac{\mu}{\mu + 5}\right], \qquad \mu = S\frac{k}{\varepsilon}, \qquad S = \sqrt{2S_{ij}S_{ij}}$$

- **k-ω models**

The standard and shear-stress transport (SST) k-ω models share similar forms, featuring transport equations for turbulent kinetic energy, k, and the specific dissipation rate, ω,. The primary distinctions between the SST model and the standard model are as follows:

- A gradual transition from the standard k-ω model in the inner region of the boundary layer to a high-Reynolds-number version of the k- ϵ model in the outer part of the boundary layer.
- A modified turbulent viscosity formulation that accounts for the transport effects of the principal turbulent shear stress.

The transport equations, methods for calculating turbulent viscosity, and procedures for determining model constants and other terms are presented separately for each model.

$$\frac{\partial}{\partial t}(\rho k) + \frac{\partial}{\partial x_j}(\rho k u_i) = \frac{\partial}{\partial x_j}\left[\Gamma_k \frac{\partial k}{\partial x_j}\right] + G_k - Y_k + S_k \tag{2.38}$$

and

$$\frac{\partial}{\partial t}(\rho \omega) + \frac{\partial}{\partial x_i}(\rho \omega u_i) = \frac{\partial}{\partial x_j}\left[\Gamma_\omega \frac{\partial \omega}{\partial x_j}\right] + G_\omega - Y_\omega + S_\omega \tag{2.39}$$

The SST k-ω model blends the standard k-ω model in the near-wall region with the standard k-ε model in the outer region using a blending function. The transport equations are similar to those of the standard k-ω model but include additional terms and blending functions to achieve the transition between the two models:

$$\frac{\partial}{\partial t}(\rho k) + \frac{\partial}{\partial x_i}(\rho k u_i) = \frac{\partial}{\partial x_j}\left[\Gamma_k \frac{\partial k}{\partial x_j}\right] + \tilde{G}_k - Y_k + S_k \tag{2.40}$$

and

$$\frac{\partial}{\partial t}(\rho\omega) + \frac{\partial}{\partial x_i}(\rho\omega u_i) = \frac{\partial}{\partial x_j}\left[\Gamma_\omega \frac{\partial \omega}{\partial x_j}\right] + G_\omega - Y_\omega + +D_\omega + S_\omega \qquad (2.41)$$

2.3.2 Solver Theory

A flow solver is a computational tool used to address fluid dynamics problems by numerically approximating the solutions to the governing equations of fluid flow, typically the Navier-Stokes equations. In this study, CFD simulations were conducted using ANSYS Fluent, which offers two numerical methods: the pressure-based solver and the density-based solver. Both methods derive the velocity field from the momentum equations. The density-based approach uses the continuity equation to obtain the density field and determines the pressure field from the equation of state. Conversely, the pressure-based approach extracts the pressure field by solving a pressure or pressure correction equation derived from the continuity and momentum equations. ANSYS Fluent solves the governing integral equations for mass and momentum conservation, and when necessary, for energy and other scalars like turbulence and chemical species. Both methods use a similar discretization process with the finite-volume method but differ in how they linearize and solve the discretized equations. Overviews of the pressure-based and density-based solution methods are shown in Figure 2.10 and Figure 2.11.

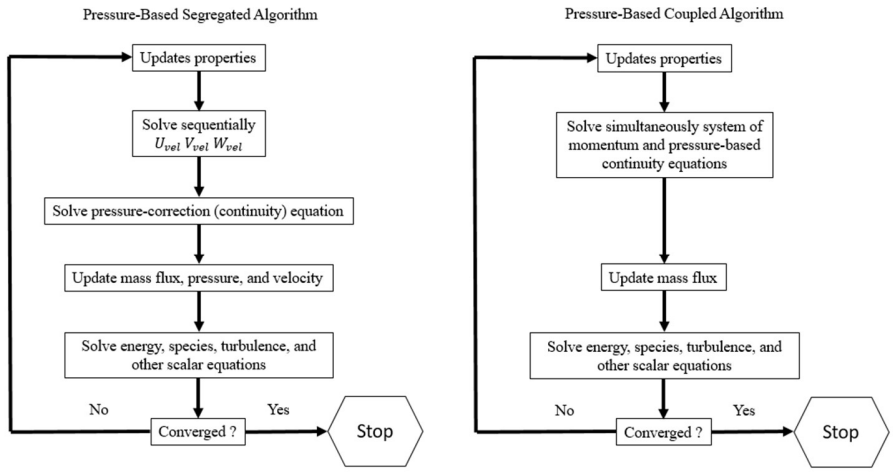

Figure 2.10: Pressure-based solution methods [28]

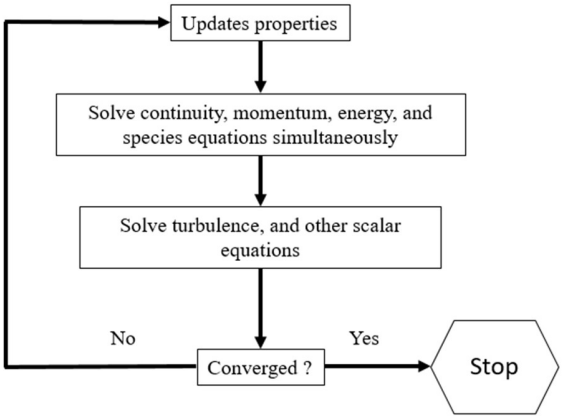

Figure 2.11: Density-based solution method [28]

2.3.3 Cavitation

Cavitation happens when the pressure in a bearing drops below the lubricant's vapor pressure, forming vapor bubbles that can collapse violently in higher pressure areas, damaging the bearing surfaces. In ANSYS Fluent, multiphase flow models are used to detect cavitation.

2.3.3.1 Multiphase Flows

Multiphase flows involve the simultaneous flow of multiple phases within a system. There are different approaches to model these flows, with two common methods being the Mixture Model and the Volume of Fluid (VOF) Method. The continuity equation for the mixture is:

$$\frac{\partial}{\partial t}(\rho_m) + \nabla.(\rho_m \overrightarrow{v_m}) = 0 \tag{2.42}$$

The momentum equation for the mixture is:

$$\frac{\partial}{\partial t}(\rho_m \overrightarrow{v_m}) + \nabla.(\rho_m \overrightarrow{v_m}\,\overrightarrow{v_m}) = -\nabla p + \nabla.\left[\mu_m\left(\nabla \overrightarrow{v_m} + \nabla \overrightarrow{v_m}^T\right)\right] + \rho_m \vec{g} + \vec{F} + \nabla.\left(\sum_{k=1}^{n} \alpha_k \rho_k \overrightarrow{v_{dr,k}}\,\overrightarrow{v_{dr,k}}\right) \quad (2.43)$$

2.4 Curve Fitting

Curve fitting is the process of finding a curve that best represents a set of data points. For example, we have data on the growth of a bacterial population over time. Let's say we measure the population size at various times, and we find that the population grows rapidly at an increasing rate. We suspect that the population growth follows an exponential model. In this case, let x be the time and y be the population size. We propose an exponential model for relationship between time and population size: $y = a.e^{bx}$. Here, a and b are the parameters to be determined through curve fitting. In curve fitting, a and b are chosen to make the model's predictions of y and x as accurate as possible. The curve fitting process can be categorized into two main types: linear and non-linear. Linear curve fitting involves straight-line relationships, while non-linear curve fitting is used to model the relationship between a dependent variable and one or more independent variables when this relationship is not linear.

Chapter 3

Methodology

To ascertain the correctness of the CFD simulations, a verification study was conducted, consulting the work of Guo et al.[24]. In their study, CFD simulations were carried out using CFX-TASC Flow and were cross-validated against the VT-EXPRESS code. VT-EXPRESS, serving as a reduced-order model, calculates the performance characteristics of hydrostatic and hydrodynamic bearings. The simulations focused on a four-recessed hybrid journal bearing, as seen in Figure 3.1. This bearing has 30 mm in diameter, 20 mm in width, and 0.03 mm clearance. Each pocket of the bearing has distinct features: an included angle of 45°, 5 mm axial land width, 1 mm pocket depth, and 0.6 mm orifice diameter. After completing the CFD simulations, a comparative analysis was performed, focusing on inlet pocket pressures, load capacity, and mass flow rates. The results of the CFD simulations matched the results obtained from VT-EXPRESS, as detailed in Table 3-1. The comparison revealed a maximum discrepancy of 2.1% in pocket inlet pressure, less than 0.5% in load capacity, and a deviation of less than 7% in mass flow rate. These findings demonstrate a high level of consistency between the current CFD results and those reported by Guo et al[24].

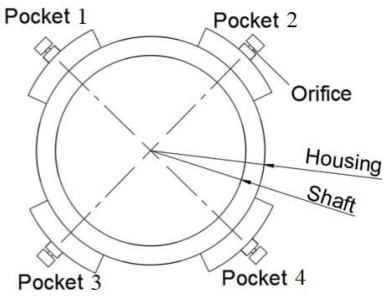

Figure 3.1: A representation of a four-pocket hybrid journal bearing

Table 3-1: A result of verification study

	Present CFD	Ref. CFD [2]	VT- Express [2]	% Diff.
Pocket 1 Inlet Pressure [MPa]	2.666	2.671	2.724	2.1
Pocket 2 Inlet Pressure [MPa]	3.699	3.723	3.745	1.2
Pocket 3 Inlet Pressure [MPa]	4.982	4.980	4.987	0.1
Pocket 4 Inlet Pressure [MPa]	4.473	4.413	4.503	0.7
Load Capacity [N]	674	727	671	0.4
Mass Flow Rate [kg/s]	0.0284	0.0318	0.0304	6.6

To evaluate the feasibility of the hybrid bearing, preliminary studies were conducted, which involved designing a candidate bearing geometry as depicted in Figure 3.2. Subsequent CFD simulations were performed to analyze its performance and determine its suitability for the intended application. These initial studies provided valuable insights into the bearing's potential and helped refine the design criteria for further development. For the analysis, nominal clearances of 100 and 300 microns were examined. The semi-cone angle was set to 45 degrees, the total length of the bearing was 70 mm, and the L/D ratio was 1. The bearing's eccentricity was set to 0.7. CFD simulations were performed with a pressure difference of 7 bars between total and static pressures, and the shaft was kept at 50000 rpm. Kerosene oil was selected as the lubricant for the simulations. The aim of the analysis was to understand key performance factors, such as the bearing's load-carrying capacity, its friction loss and cavitation areas. The detailed Fluent setup is shown in Table 3-2. This turbulence model was validated prior to its use in the simulations. A hexahedral mesh structure was used as shown in Figure 3.3.

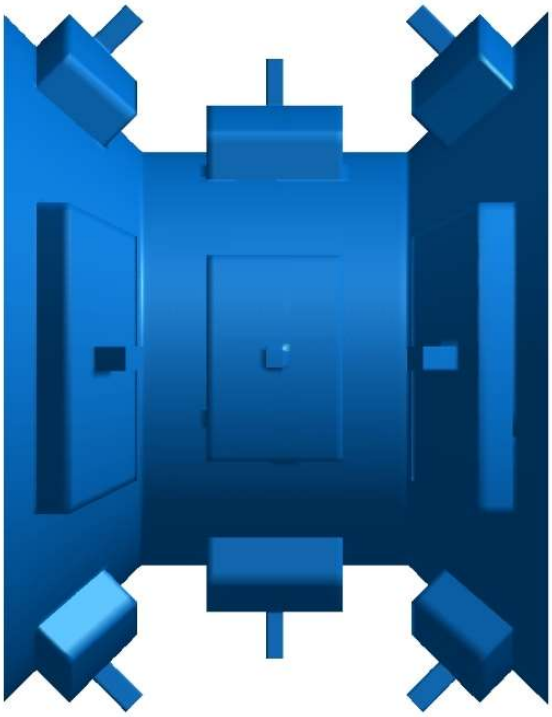

Figure 3.2: The entire hybrid bearing geometry

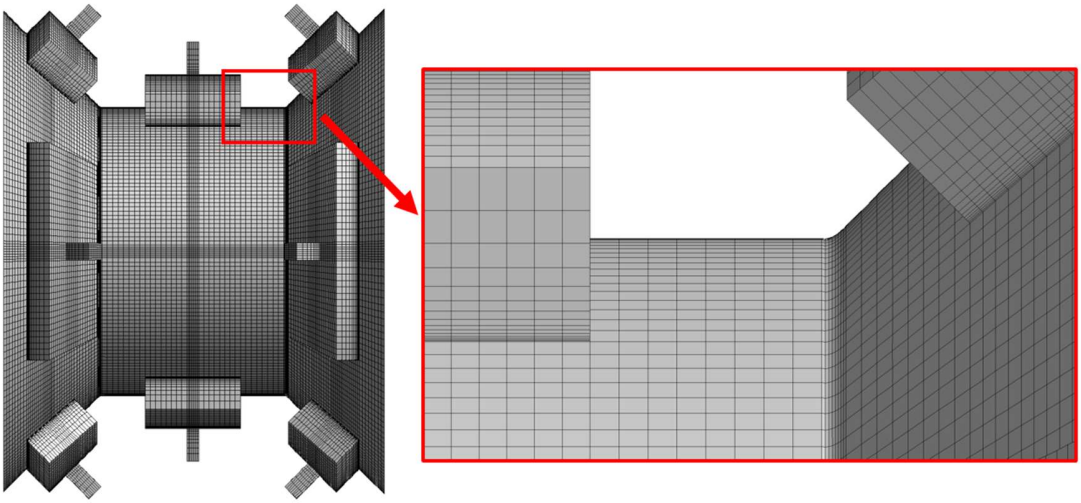

Figure 3.3: A mesh structure of the hybrid bearing geometry

Table 3-2: Ansys FLUENT setup

Multiphase model	Mixture
	Phase-1: kerosene-liquid
	Phase-2: kerosene-vapor
Cavitation model	Zwart-Gerber-Belamri
Vaporization Pressure	700 Pascal
Viscous Model	Realizable k-epsilon Enhanced Wall Treatment
Scheme	SIMPLEC
Gradient	Green-Gauss Node Based
Pressure	PRESTO!
Momentum	Second Order Upwind
Volume Fraction	First Order Upwind
Turbulent Kinetic Energy	Second Order Upwind
Turbulent Dissipation Ratio	Second Order Upwind

To address the impracticality of performing CFD simulations for every configuration, a Design of Experiments (DOE) study was conducted. This study aimed to predict bearing performance parameters efficiently by systematically exploring different design variables and their impacts, thereby reducing the need for extensive CFD simulations.

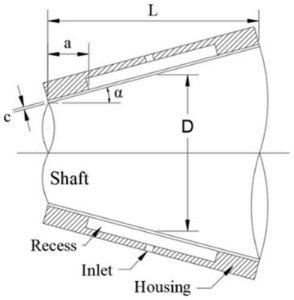

Figure 3.4: A Single Cone Bearing Geometry [27]

Deriving equations for radial and axial load capacities, friction losses, and volume flow rate presented significant challenges. To tackle this, the Buckingham Pi Theorem was employed to nondimensionalize the equations, thereby reducing the number of parameters. The key parameters considered for the bearing operation include:

- Axial bearing land width (a),
- Length of the bearing (L),
- The mean diameter of the shaft (D),
- Tangential speed at the mean radius (U),
- Total-to-static pressure difference (ΔP),
- Dynamic viscosity (μ),
- Density (ρ),
- Semi cone angle (α),
- Nominal clearance (c),
- Radial load capacity (W_R),
- Axial load capacity (W_A),
- ,Friction loss (F)
- Volume flow rate (Q)

The relationship between dimensional parameters was defined as follows:

$$W_R, W_A, F, Q = (a, L, D, U, c, \rho, \mu, \Delta P, \alpha) \tag{3.1}$$

By applying the Buckingham Pi Theorem, these parameters were nondimensionalized, which simplified the analysis and allowed for a more efficient evaluation of the bearing's performance. The Pi groups were derived as non-dimensional parameters to analyze the functional relationships between various performance metrics. The functional relationships considered are between the friction coefficient ($\overline{F}$), radial load capacity

coefficient ($\overline{W_R}$), axial load capacity coefficient ($\overline{W_A}$) and flow coefficient ($\overline{Q}$). The relationships can be expressed as:

$$\overline{F}, \overline{W_R}, \overline{W_A}, \overline{Q} = f(\Pi_1, \Pi_2, \Pi_3, \Pi_4, \Pi_5, \Pi_6) \tag{3.2}$$

$$\Pi_1 = \frac{a}{L} \tag{3.3}$$

$$\Pi_2 = \frac{L}{D} \tag{3.4}$$

$$\Pi_3 = \alpha \tag{3.5}$$

$$\Pi_4 = \frac{c}{D} \tag{3.6}$$

$$\Pi_5 = \frac{\rho U c}{\mu} \tag{3.7}$$

$$\Pi_6 = \frac{\Delta P}{\frac{1}{2}\rho U^2} \tag{3.8}$$

$$\overline{F} = \frac{F}{\frac{1}{2}\rho U^3 D L} \tag{3.9}$$

$$\overline{W_R} = \frac{W_R}{\frac{1}{2}\rho U^2 \pi D \frac{L}{cos(\alpha)}} \tag{3.10}$$

$$\overline{W_A} = \frac{W_A}{\frac{1}{2}\rho U^2 \pi D \frac{L}{cos(\alpha)}} \tag{3.11}$$

$$\overline{Q} = \frac{Q}{UD^2} \tag{3.12}$$

Before conducting the CFD simulations, the non-dimensional parameters were set to three different levels, as illustrated in the Table 3-3. This step was crucial for systematically exploring the parameter space and understanding their effects on the bearing's performance. By varying these parameters across different levels, the study aimed to capture a comprehensive range of operational scenarios and derive meaningful insights from the simulations.

Table 3-3: Levels of Pi groups

Level	Π_1	Π_2	Π_3	Π_4	Π_5	Π_6
1	0.1	0.5	0	0.001429	11912	0.053
2	0.15	0.75	15	0.002857	29780	0.084
3	0.25	0.875	30	0.004286	47647	0.107

In a full factorial design, obtaining information about interactions would require conducting 3^6=729 experiments. To mitigate this extensive experimentation, the Taguchi method [29] was employed. Specifically, Taguchi's L27 orthogonal array was utilized, as detailed in Table 3-3. This L27 array is designed to accommodate six factors, each at three levels, thereby significantly reducing the number of required experiments from 729 to just 27 as depicted in Table 3-4. After completing the 27 CFD runs, the Mathematica tool was used for curve fitting. The NonLinearModelFit function was applied to this data set, resulting in the creation of meta-models for the four different bearing coefficients. These meta-models captured both the coefficients and the nonlinear relationships between the input and output parameters, providing a simplified and efficient way to predict bearing performance based on the derived non-dimensional parameters.

Table 3-4: Taguchi's L27 Orthogonal Array

Test	Π_1	Π_2	Π_3	Π_4	Π_5	Π_6
1	1	1	1	1	1	1
2	1	1	1	1	2	2
3	1	1	1	1	3	3
4	1	2	2	2	1	1
5	1	2	2	2	2	2
6	1	2	2	2	3	3
7	1	3	3	3	1	1
8	1	3	3	3	2	2
9	1	3	3	3	3	3
10	2	1	2	3	1	2
11	2	1	2	3	2	3
12	2	1	2	3	3	1
13	2	2	3	1	1	2
14	2	2	3	1	2	3
15	2	2	3	1	3	1
16	2	3	1	2	1	2
17	2	3	1	2	2	3
18	2	3	1	2	3	1
19	3	1	3	2	1	3
20	3	1	3	2	2	1
21	3	1	3	2	3	2
22	3	2	1	3	1	3
23	3	2	1	3	2	1
24	3	2	1	3	3	2
25	3	3	2	1	1	3
26	3	3	2	1	2	1
27	3	3	2	1	3	2

For the experimental study, a cylindrical hydrodynamic bearing test rig was designed in the Turbomachinery and Heat Transfer Lab at Technion-IIT as shown in Figure 3.5 and Figure 3.6. The rotor has 75 mm diameter, 100 mm length, and 300 micron nominal clearance.

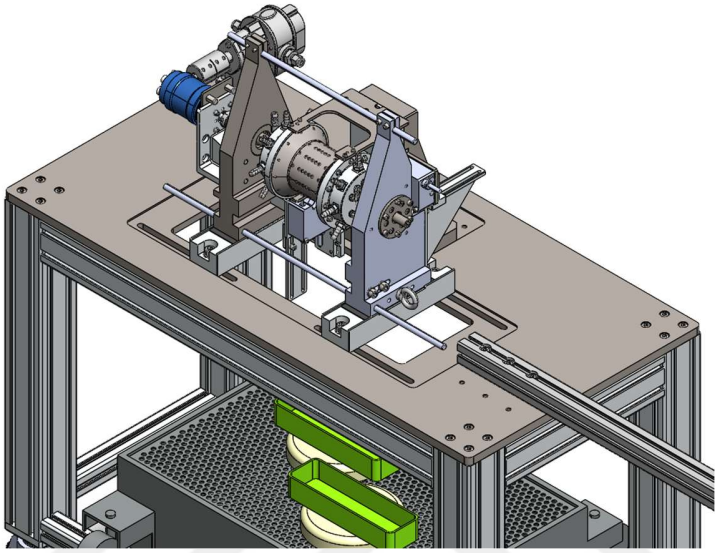

Figure 3.5: A bearing test rig

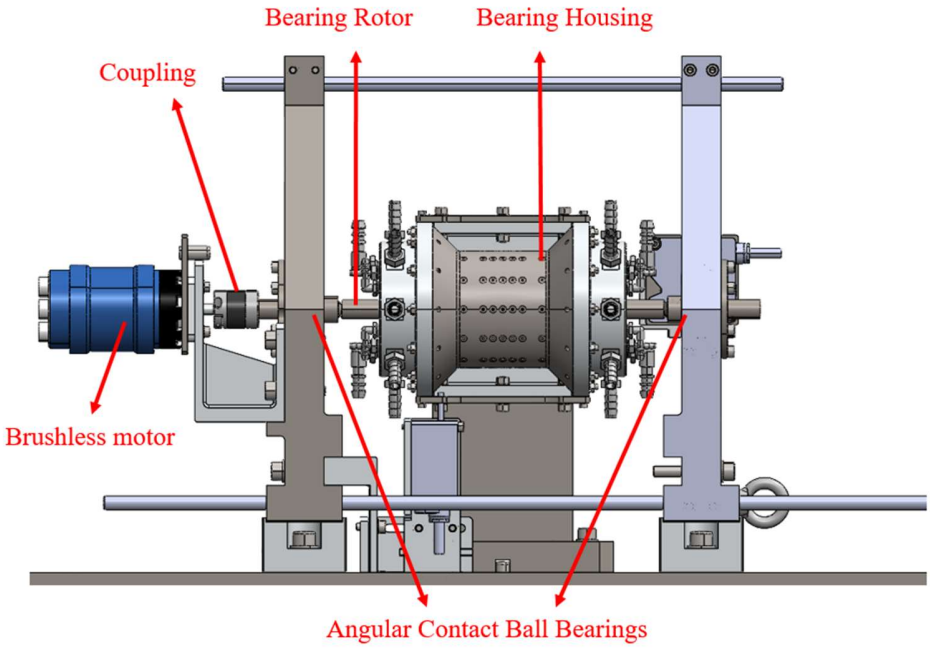

Figure 3.6: The bearing test rig

A Turnigy AquaStar T20 3T 730KV/1280 KV water-cooled brushless motor was connected to the bearing rotor using a coupling to provide rotational movement. The brushless motor was connected to a Flipsky FSESC 75350 controller, which was used for precise control of the motor's operation. This advanced controller has the capability to measure and monitor various parameters, including RPM, current, and power loss, providing valuable data for the experimental study. The power for the system was supplied by a Wemaxpower DC power supply, ensuring stable and reliable electrical input for the brushless motor and controller. To ensure the rotor remained steady during its movement, angular contact ball bearings were employed. On the bearing housing, 112 pressure holes were drilled, arranged in 16 circumferential columns and 7 rows. These pressure holes were connected to a Scanivalve DSA3207 pressure scanner, which was utilized to measure static pressure. The pressure scanner was managed using its proprietary software, enabling precise measurement and recording of static pressure data. To measure pressure on the sides, four Huba Control Differential Pressure Transmitter 692 units were employed. Voltage readings from these transmitters were converted into pressure measurements in bars using a LabVIEW code specifically developed for this task as shown in Figure 3.7. Additionally, eight thermocouples were connected to the test rig and integrated into the same LabVIEW code. This arrangement enabled simultaneous measurement and monitoring of both pressure and temperature throughout the test rig. Experiments were conducted using two different lubricants: water and kerosene. For the water experiments, two simple water pumps were utilized, each providing a flow rate of 3000 L/h. In the kerosene experiments, two fuel pumps, controlled by a separate power supply, were employed. The lubricants were supplied from the sides. The final configuration of the bearing test rig is shown in Figure 3.8.

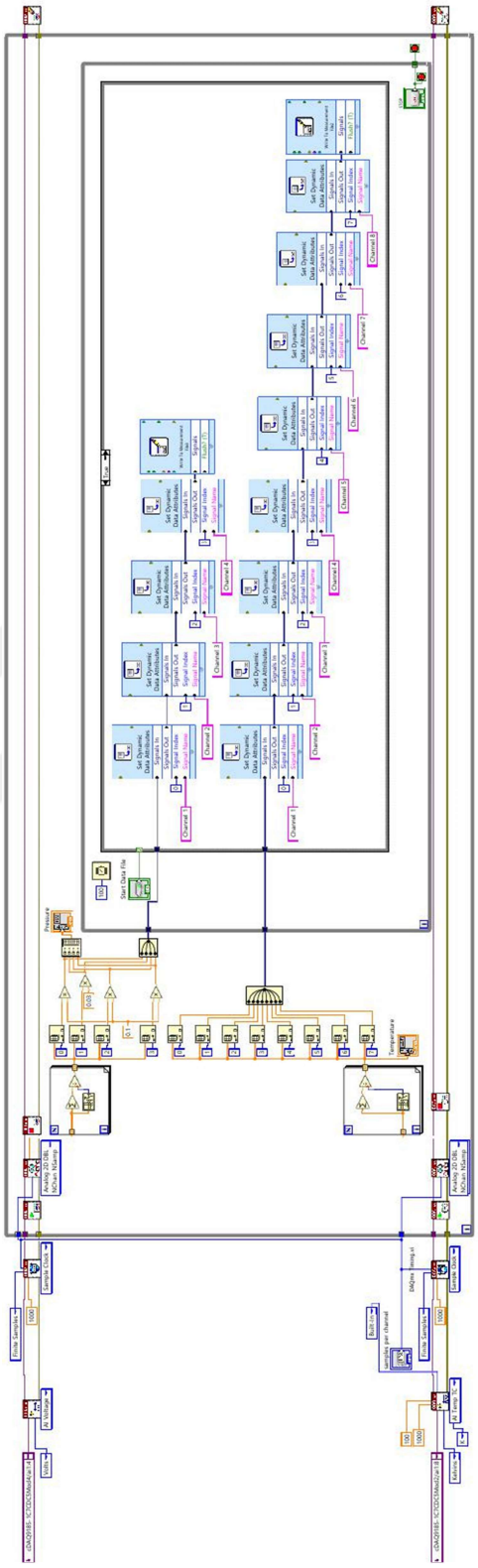

Figure 3.7: A LabVIEW code for pressure and temperature measurement

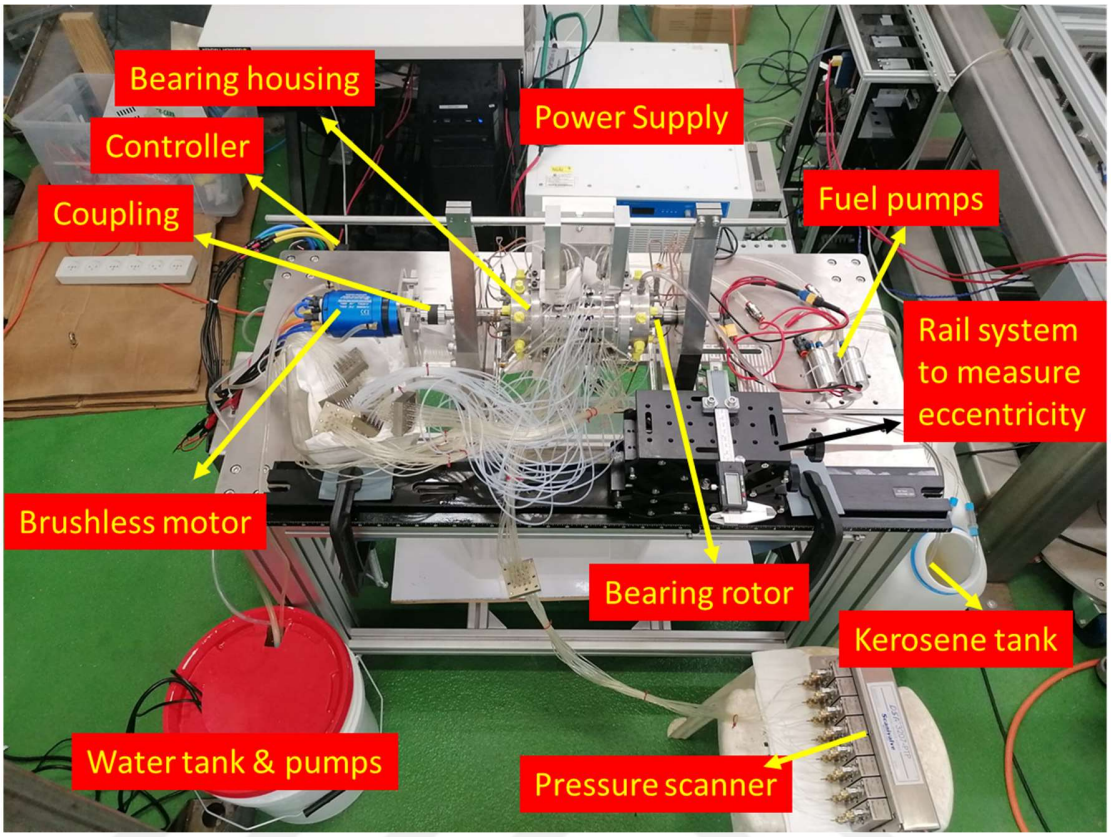

Figure 3.8: The hydrodynamic journal bearing test rig

Chapter 4

Results

4.1 Entire Bearing Geometry Overview

In the flow field, some regions of the lubricating fluid encounter pressure drops below the vapor pressure as the fluid moves from the recess areas to the landing zones. This pressure drop leads to cavitation, where the fluid undergoes a phase transition into vapor, forming tiny gas bubbles. As depicted in Figure 4.1, cavitation areas can be seen.

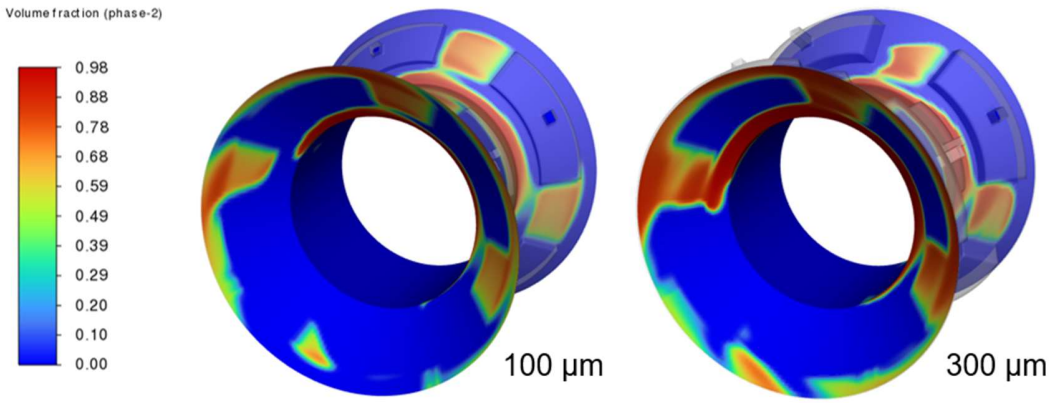

Figure 4.1: Cavitation areas

On the other hand, areas under recesses experience elevated shear stress, as shown in Figure 4.2, resulting in increased friction and more intense circulation. These observations suggest that classical hydrodynamic theory is inadequate for large-clearance hybrid bearings.

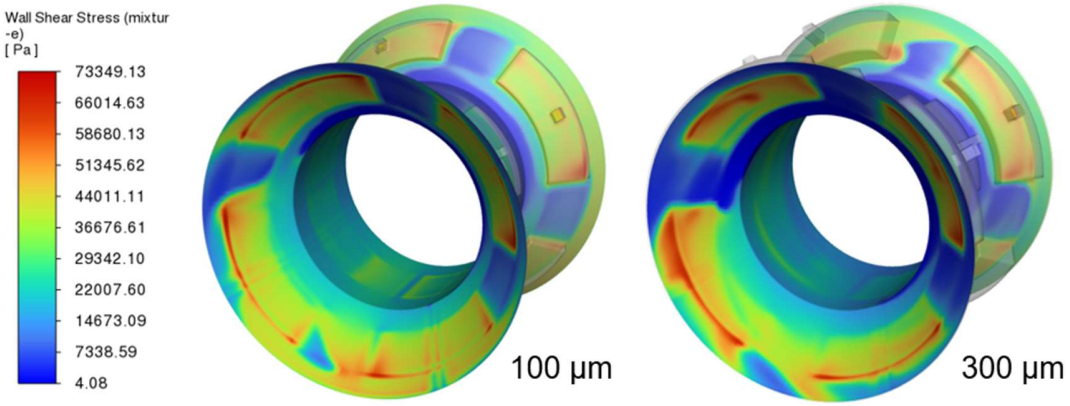

Figure 4.2: Wall shear stresses

Figure 4.3 illustrates the pressure distributions on the bearing's shaft surface. The compressor side exhibits lower pressure relative to the turbine side, primarily due to the lack of a flow exit on the turbine side. Furthermore, areas affected by cavitation display lower pressure levels.

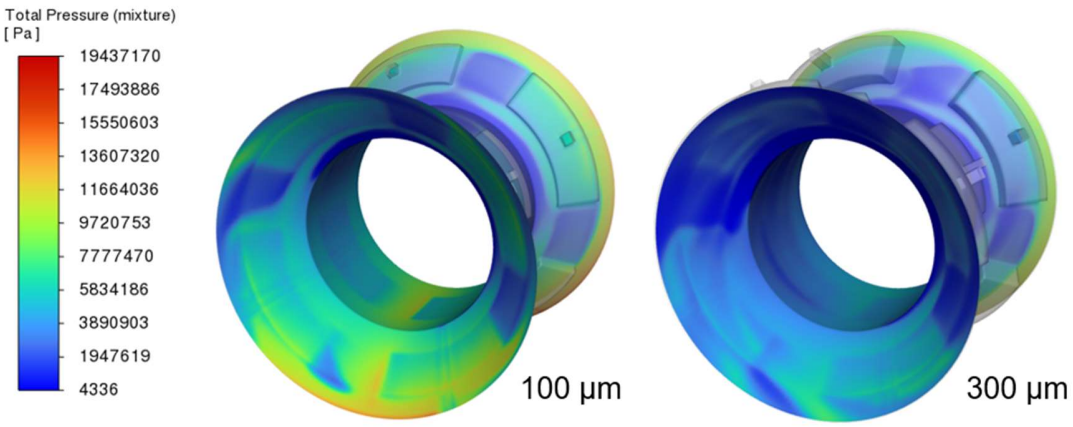

Figure 4.3: Pressure distributions

Figure 4.4 depicts the flow vectors within the system. Figure 4.4A shows fluid moving upward on the turbine-side bearing due to shaft rotation, though it should ideally flow downward toward the compressor side. Figure 4.4B highlights strong circulatory motion and transverse velocity gradients in the pocket, increasing friction. Finally, Figure 4.4C

demonstrates flow uniformity from rotational acceleration, reducing skin friction on the shaft surface.

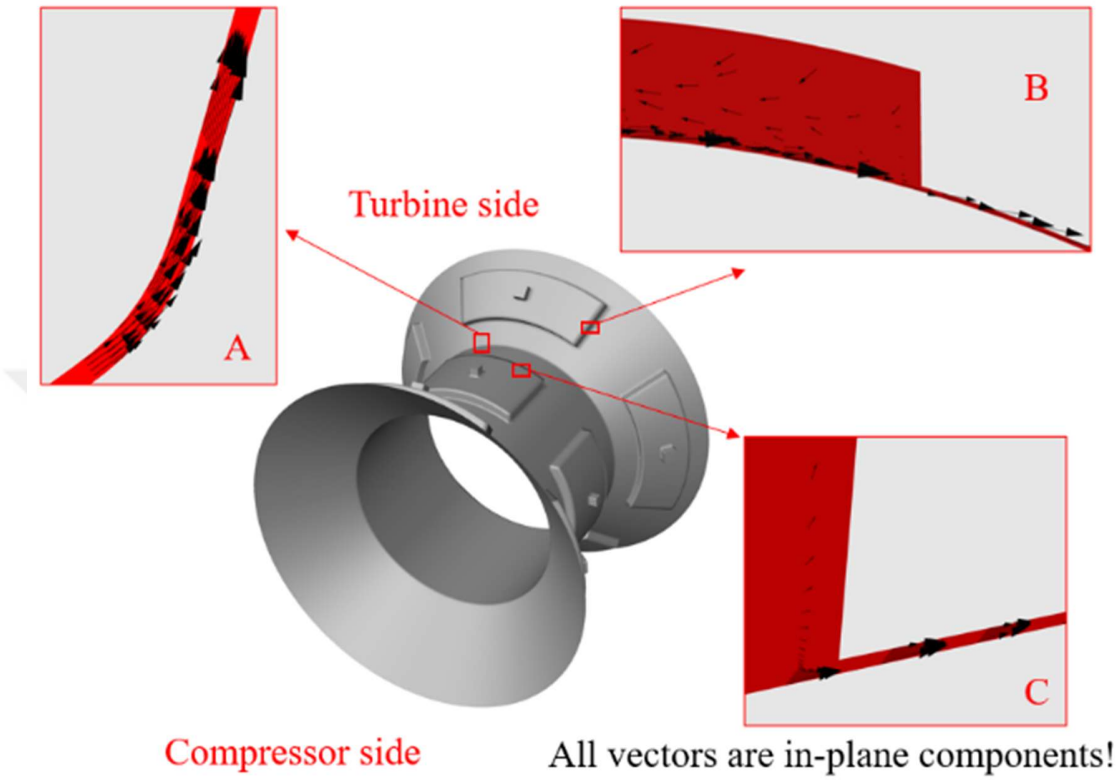

Figure 4.4: Bearing's fluid velocity field

Figure 4.5 and Figure 4.6 evaluate the bearing's overall performance. Figure 4.5 shows that 300 micron case reduces radial load support but improves axial load capacity. Figure 4.6 reveals that increasing the landing gap from 100 to 300 microns cuts friction power loss by about 10%. Reducing surface area lowers power consumption but can compromise load capacity, which can be mitigated by raising oil pressure in recesses.

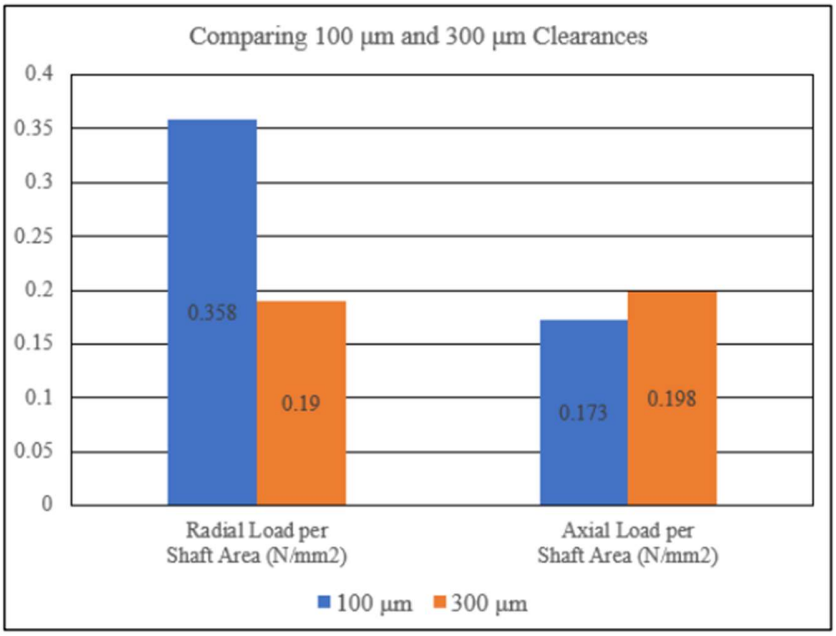

Figure 4.5: Comparison of load carrying capacity per shaft area

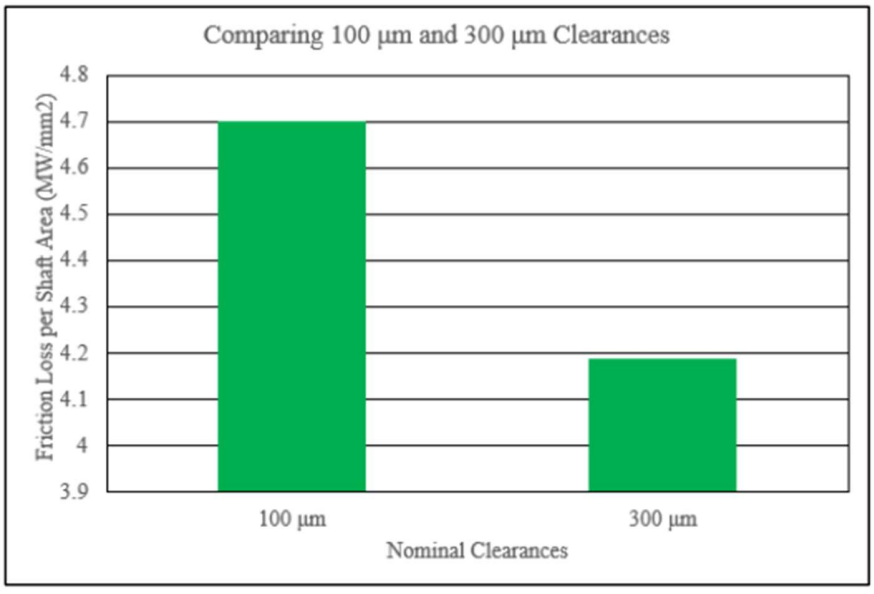

Figure 4.6: Comparison of friction losses per shaft area

4.2 Design of Experiment (DoE)

Five distinct mesh configurations, ranging from coarse Mesh-1 to fine Mesh-5, were developed and evaluated, as illustrated in Figure 4.7. The mesh densities varied from elements for the coarsest configuration to elements for the finest. Mesh-4 was selected as it provided a suitable balance between computational efficiency and accuracy, with only a 6% difference in results compared to the highest-resolution Mesh-5. For discretizing the fluid domain, a hexahedral mesh structure was created. The number of layers was adjusted according to clearance size: 48 layers for a 300 µm clearance, 32 layers for a 200 µm clearance, and 16 layers for a 100 µm clearance.

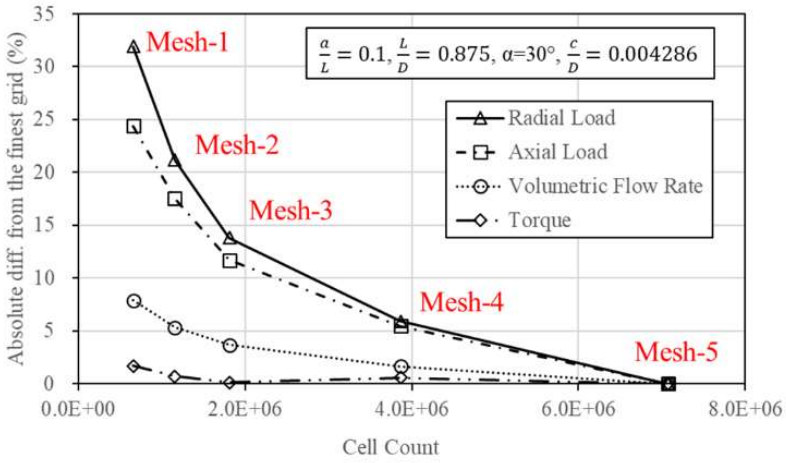

Figure 4.7: Mesh sensitivity analysis

The CFD simulation revealed that in certain localized areas cavitation occurs during the transition from recess to landing zones due to acceleration. This pressure reduction causes the fluid to vaporize, resulting in cavitation. Cavitation reduces skin friction in the landing regions, as shown in Figure 4.8 and Figure 4.9. Additionally, the acceleration in these regions helps to standardize the tangential flow, as depicted in Figure 4.10B, which further reduces skin friction on the shaft surface. In contrast, the interaction between the stationary deep recess and the high-speed tangential velocity of the shaft creates intense circulation and vortical flow, leading to increased shear in the recess regions compared to

the landing zones, as illustrated in Figure 4.10A. As a result, the bearing exhibited a power consumption of up to 46 kW.

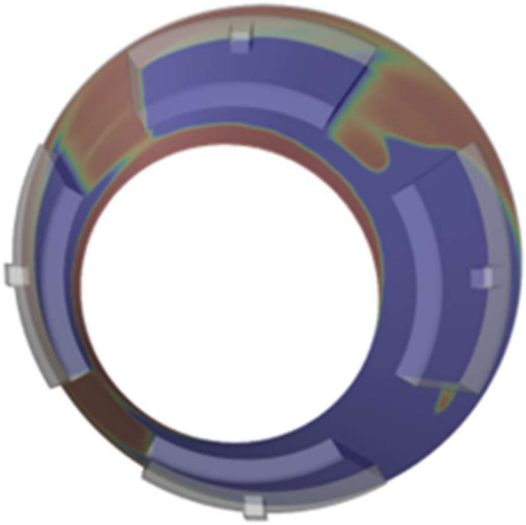

Figure 4.8: Represantation of cavitation zones by vapor volume fraction

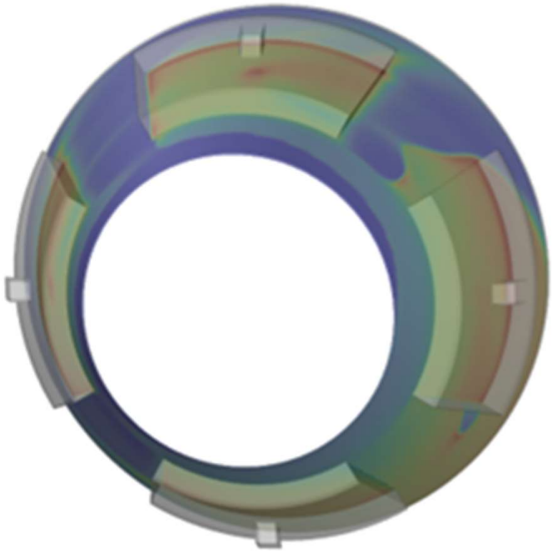

Figure 4.9: Skin friction on the shaft surface

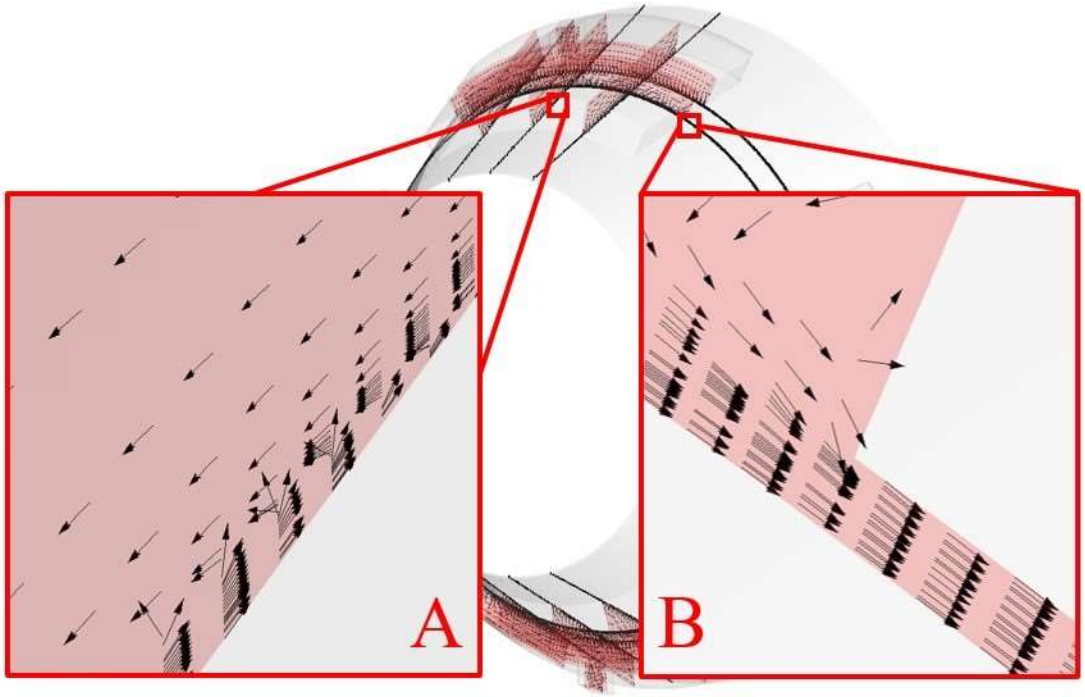

Figure 4.10: Velocity vectors of the lubricant

The analysis conducted revealed substantial discrepancies between conventional hydrodynamic theory and the bearing configuration under investigation. These differences can be attributed to the unusually high shaft tangential velocity and the increased bearing clearance, both of which result from the specific engine components and the constraints of additive manufacturing. For the nonlinear regression analysis, each dimensionless parameter was evaluated individually in relation to the coefficients. The goal was to establish the relationship between these coefficients and the dimensionless values. This means that one of the Pi groups was varied while keeping the others constant as shown in Figure 4.11, Figure 4.12, Figure 4.13 and Figure 4.14.

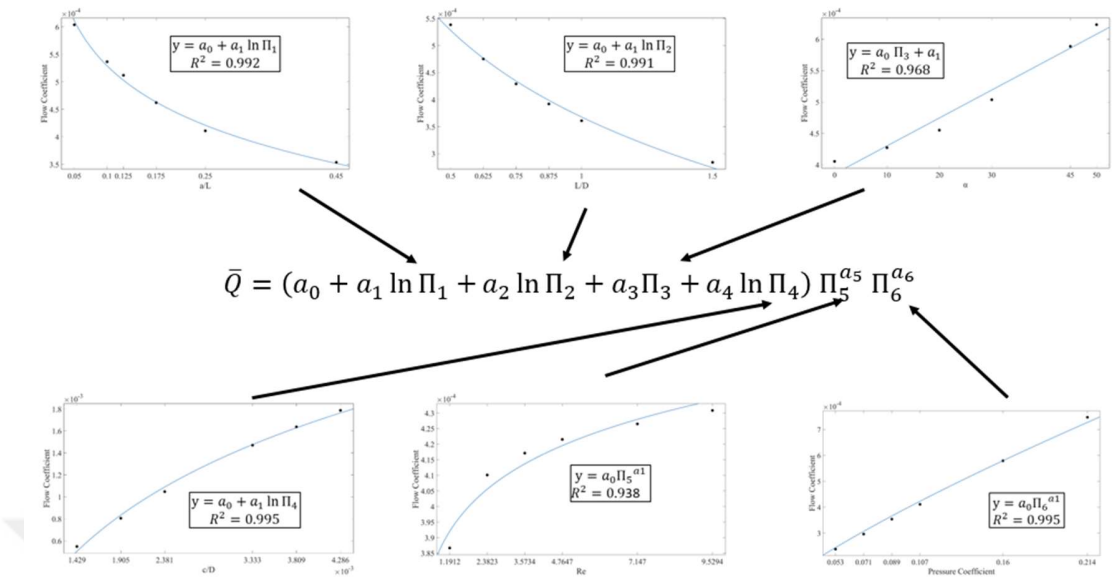

Figure 4.11: Pi groups and Flow Coefficient

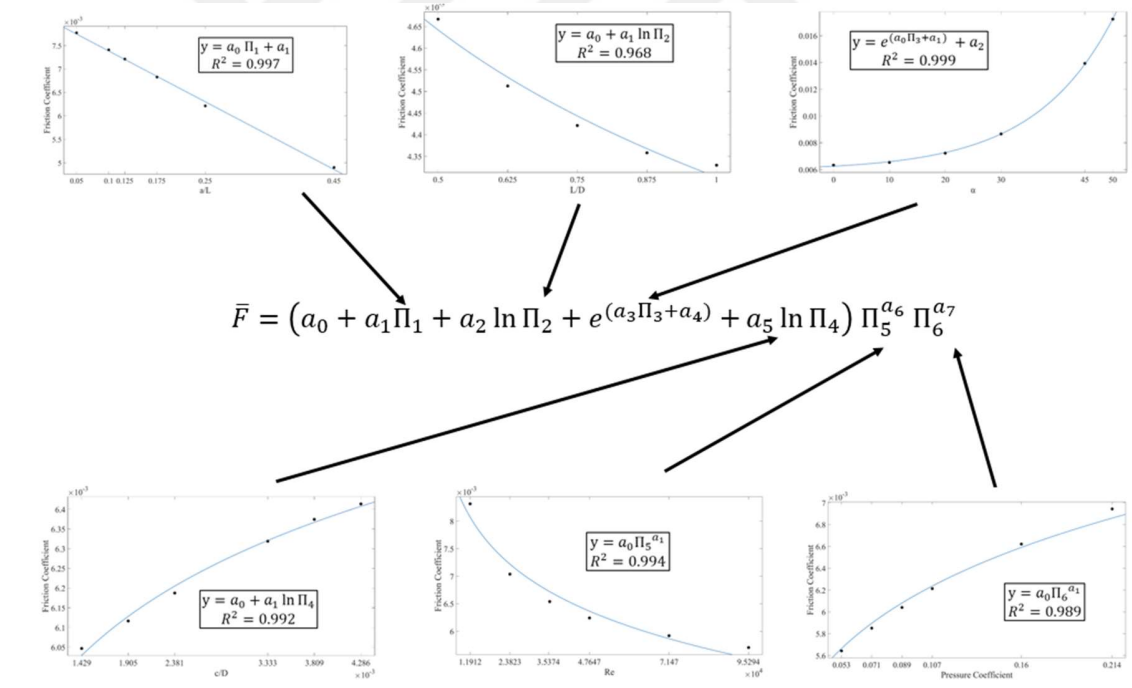

Figure 4.12: Pi groups and Friction Coefficient

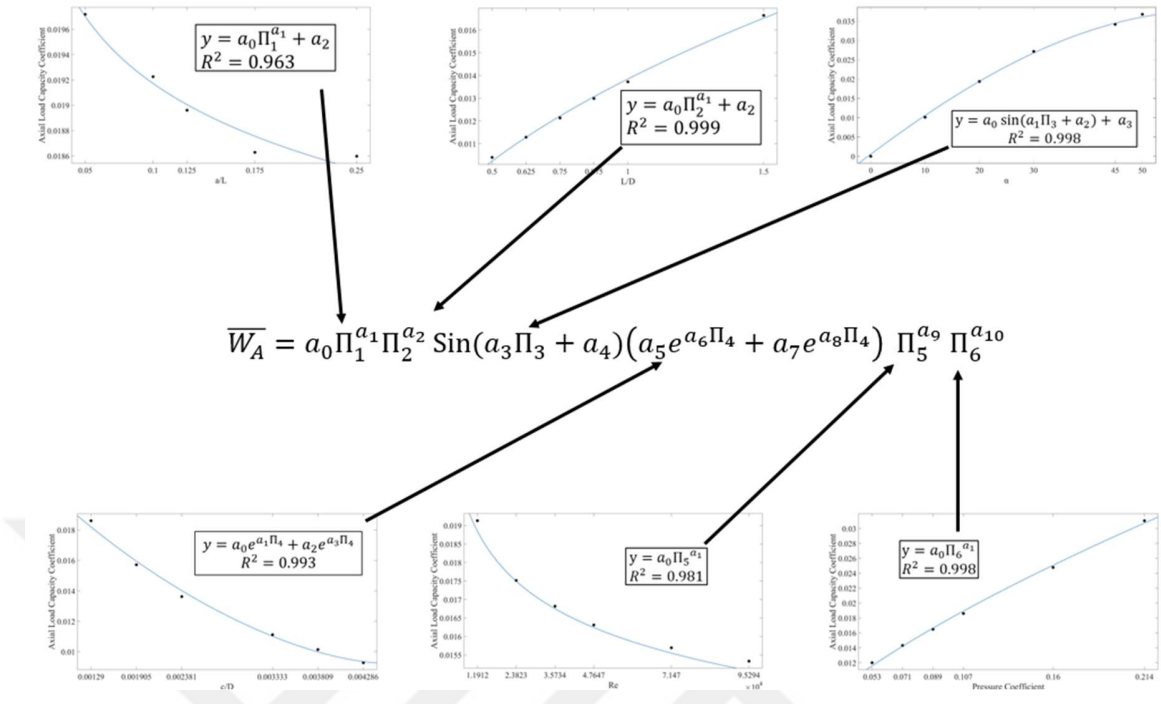

Figure 4.13: Pi groups and Axial Load Coefficient

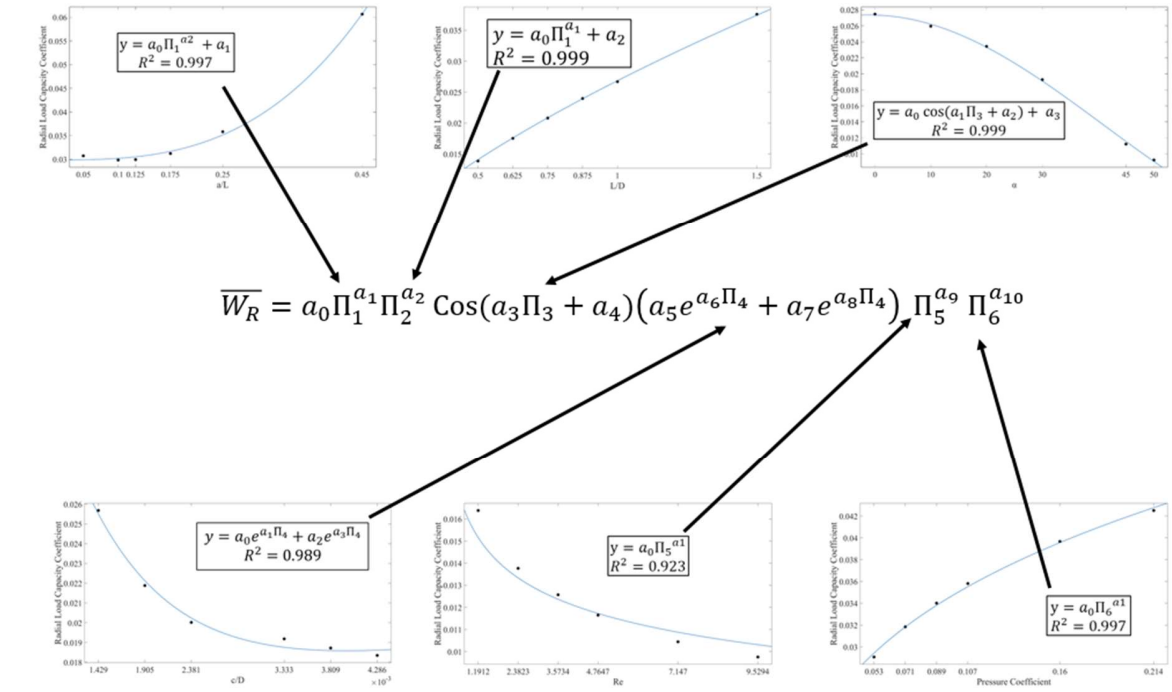

Figure 4.14: Pi groups and Radial Load Coefficient

To validate the developed model, additional CFD simulations were performed for the Pi groups at the three levels defined by Taguchi's method used during model development. The CFD results were compared with the model's predicted values. Figure 4.15, Figure 4.16, Figure 4.17 and Figure 4.18 display the outcomes of this comparison, with empty markers indicating the additional CFD simulations. The results show that the meta-model effectively predicts the trends observed in the CFD data. Friction, flow, axial load and radial load capacities are obtained as:

$$\bar{F} = (0.0881607 - 0.10345\prod_1 - 0.00385156\, log\prod_2 + e^{(-6.72114+0.0963311\prod_3)} - 0.000606793\prod_4)\prod_5^{0.1759}\prod_6^{-0.217317} \quad (4.1)$$

$$\bar{Q} = (0.0134436 - 0.000527007\, log\prod_1 - 0.00095007\, log\prod_2 + 0.0000136716\prod_3 + 0.00209433\prod_4)\prod_5^{0.08127}\prod_6^{0.704837} \quad (4.2)$$

$$\overline{W_A} = 0.402357\prod_1^{-0.201262}\prod_2^{0.0511532}\, sin\prod_3\big(\ \ 1.98758e^{(-464.33\prod_4)} + \ \ 0.0610629\, e^{(278.403\prod_4)}\big)\prod_5^{-0.102456}\prod_6^{0.866468} \quad (4.3)$$

$$\overline{W_R} = -1.21129\prod_1^{0.0183368}\prod_2^{0.852324}\, cos(-10.8662 + 2.07373\prod_3)\ \big(-0.849931e^{-64\ .799\prod_4} - 0.291297e^{74.6161\prod_4}\big)\prod_5{}^{-0.201902}\prod_6{}^{0.448238} \quad (4.4)$$

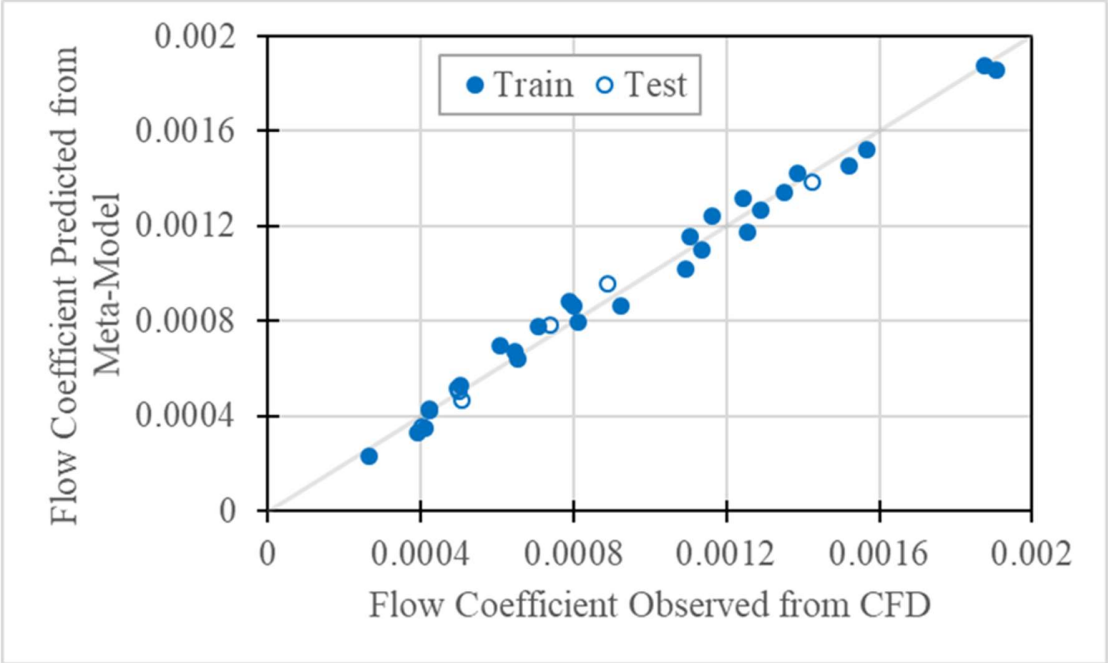

Figure 4.15: Predicted and observed flow coefficients from meta-model and CFD

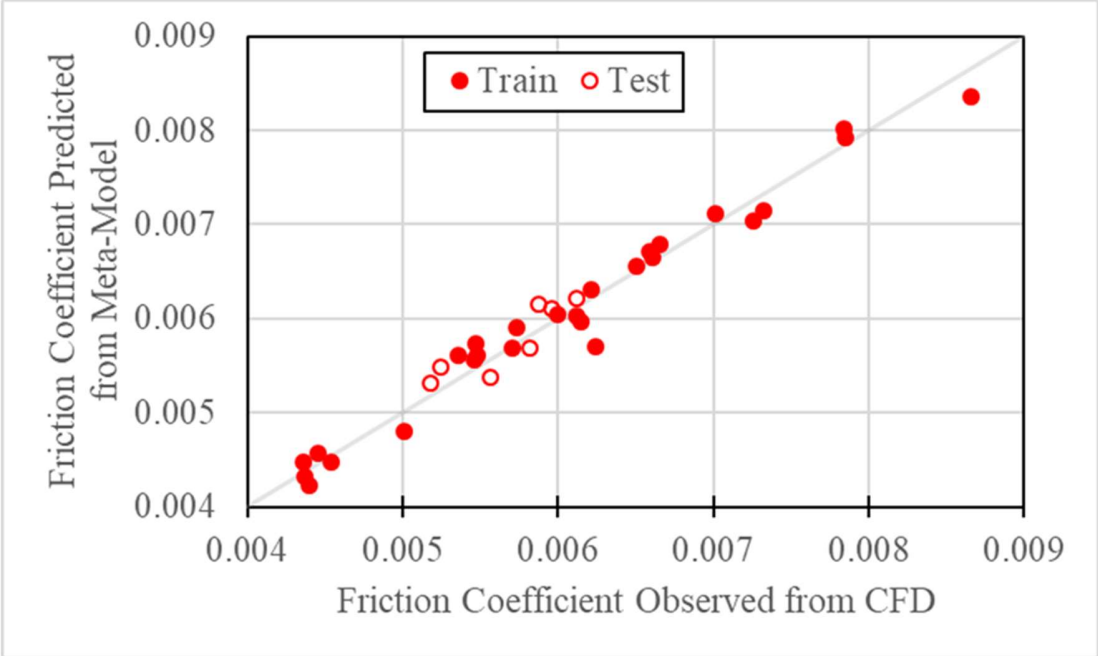

Figure 4.16: Predicted and observed friction coefficients from meta-model and CFD

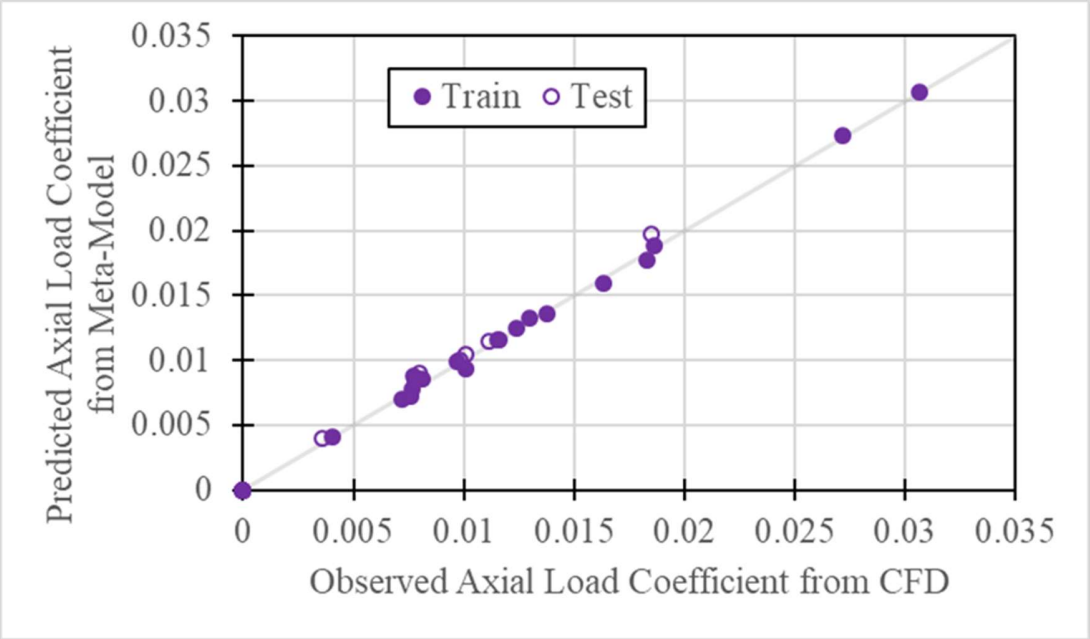

Figure 4.17: Predicted and observed axial load capacity coefficients from meta-model and CFD

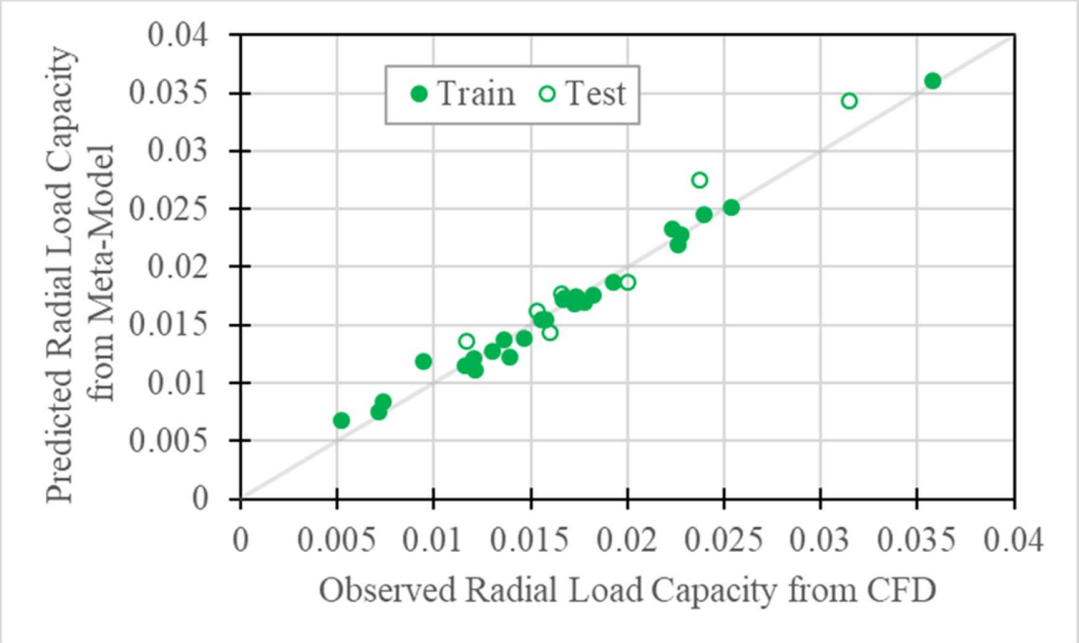

Figure 4.18: Predicted and observed radial load capacity coefficients from meta-model and CFD

4.3 A Hydrodynamic Bearing Test Rig

Experiments were conducted on the cylindrical hydrodynamic test rig using two different lubricants: water and kerosene. These tests were carried out at various rotational speeds to assess the performance of the bearing under different conditions. Since there is no recess or pressurized lubricant supply, this bearing functioned purely as a hydrodynamic bearing, with pressure generation solely dependent on the bearing's rotation. As the shaft rotates within the cylindrical bearing, the lubricant is drawn into the gap between the rotor and housing. The rotation generates pressure to support the shaft. CFD simulations were conducted for this case as shown in Figure 4.19.

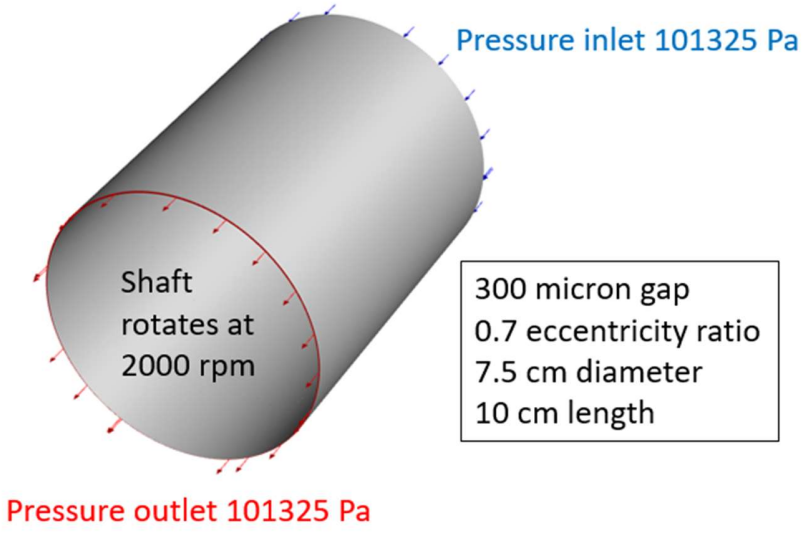

Figure 4.19: Boundary conditions

As shown in Figure 4.21, results from CFD and experiments matched with the trends observed in the full-Sommerfeld regime, similar to those seen in conventional hydrodynamic bearings as depicted in Figure 4.20. A noticeable deviation is observed between the 8th and 12th pressure points. Possible reasons for this discrepancy include the growth of air bubbles at these points, inadequate drainage in the pipes, or potential damage to the pipes.

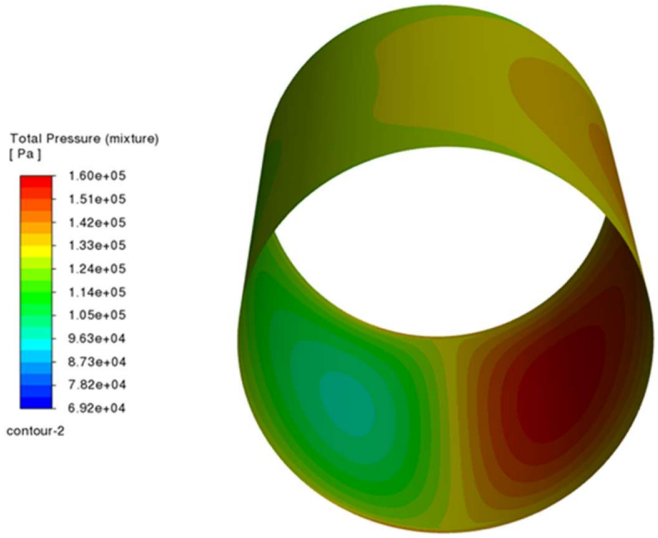

Figure 4.20: Pressure distribution of the water lubricated bearing at 4000 rpm

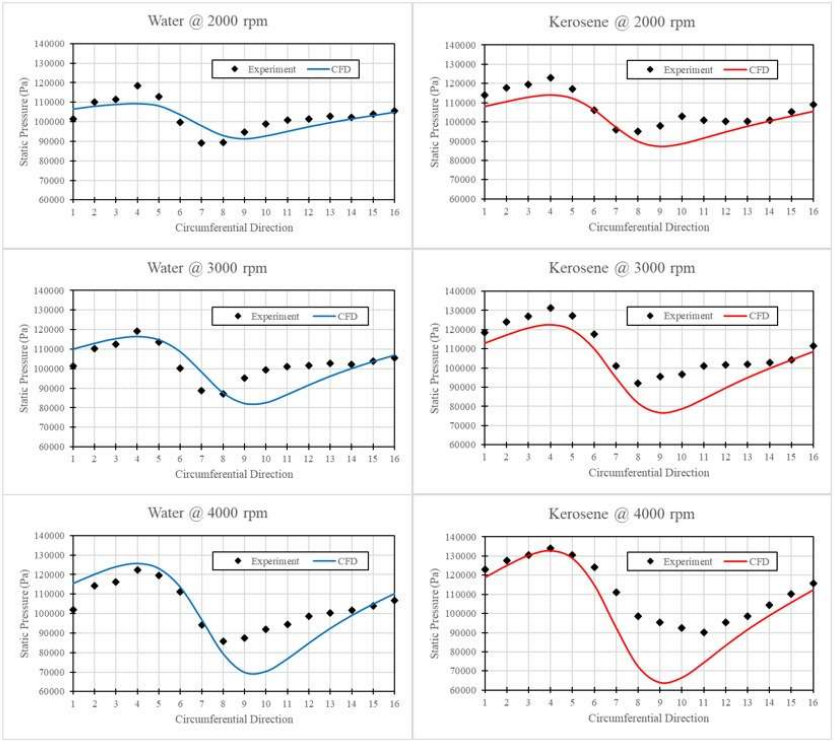

Figure 4.21: A comparison of static pressures at various rotational speed

Chapter 5

Conclusion

In this study, the primary objective was to investigate hydrostatic and hydrodynamic bearings utilized in small gas turbines through both numerical simulations and experimental validation. The research focused on assessing the performance and feasibility of these bearings, particularly in the context of additive manufacturing. The proposed design, intended for production using additive manufacturing techniques, introduced specific design constraints, including a higher nominal gap compared to traditional manufacturing methods. Two different bearing analyses were conducted with clearances of 100 and 300 microns, an L/D ratio of 1. Due to the limitations of additive manufacturing, the bearing has an unconventionally high clearance gap. As a result, initial CFD analysis of the bearing revealed significant discrepancies between CFD results and hydrodynamic bearing theory. To address this, Taguchi's L27 orthogonal array DoE was implemented with six independent Pi groups of the bearing's geometrical properties. Non-linear regression was applied to the simulation results to form correlations between bearing performance and its geometry. The resulting mathematical model can serve as a guideline during the preliminary design stage. Additionally, a cylindrical hydrodynamic bearing test rig was created, and experimental studies were conducted using two different viscosities. It was observed that the CFD results and the experimental data closely matched each other, validating the numerical simulations. The findings from this study contribute valuable insights into the integration of additive manufacturing in bearing design, highlighting both the opportunities and challenges associated with this innovative approach. The results underscore the potential benefits of additive manufacturing for custom bearing solutions while also identifying areas for further research to address the associated design constraints.

References

[1] K. J. Stout & W. B. Rowe (1974). Externally pressurized bearings - design for manufacture Part 1 — journal bearing selection. *Tribology*, 7(3), 98–106. doi: 10.1016/0041-2678(74)90009-8.

[2] A. A. Raimondi & J. Boyd (1958). A Solution for the Finite Journal Bearing and its Application to Analysis and Design: I. *A S L E Trans.*, 1(1), 159–174. doi: 10.1080/05698195808972330.

[3] J. P. O'Donoghue, W. B. Rowe & C. J. Hooke (1969). Design of hydrostatic bearings using an operating parameter. *Wear*, 14(5), 355–362. doi: 10.1016/0043-1648(69)90016-7.

[4] L. J. Nypan, B. J. Hamrock, H. W. Scibbe & W. J. Anderson (1972). Optimization of Conical Hydrostatic Bearing for Minimum Friction. *J. Lubr. Technol.*, 94(2), 136–142. doi: 10.1115/1.3451656.

[5] L. San Andres, D. Childs & Z. Yang (1995). Turbulent-flow hydrostatic bearings: Analysis and experimental results. *Int. J. Mech. Sci.*, 37(8), 815–829. doi: 10.1016/0020-7403(94)00104-R.

[6] S. C. Sharma, V. M. Phalle & S. C. Jain (2011). Performance analysis of a multirecess capillary compensated conical hydrostatic journal bearing. *Tribol. Int.*, 44(5), 617–626. doi: 10.1016/j.triboint.2010.12.012.

[7] X. B. Zuo, J. M. Wang, Z. Q. Yin & S. Y. Li (2013). Performance analysis of multirecess angled-surface slot-compensated conical hydrostatic bearing. *J. Tribol.*, 135(4), 1–10. doi: 10.1115/1.4024296.

[8] J. Wang, J. Huang, S. Jiang, A. N. Kouediatouka, Q. Liu & G. Dong (2023). Analysis of maximum radial load capacity of hydrostatic journal bearing considering supply pressure limitation by a novel method. *Tribol. Int.*,184, 108484. doi: 10.1016/j.triboint.2023.108484.

[9] A. A. Raimondi & J. Boyd (1958). A Solution for the Finite Journal Bearing and its Application to Analysis and Design: II. *A S L E Trans.*, 1(1), 175–193. doi: 10.1080/05698195808972330.

[10] A. A. Raimondi & J. Boyd (1958). A Solution for the Finite Journal Bearing and its Application to Analysis and Design: III. *A S L E Trans.*, 1(1), 194–209. doi: 10.1080/05698195808972330.

[11] B. Manser, I. Belaidi, A. Hamrani, S. Khelladi & F. Bakir (2019). Performance of hydrodynamic journal bearing under the combined influence of textured surface and journal misalignment: A numerical survey. *Comptes Rendus. Mécanique*, 347(2), 141–165. doi: 10.1016/j.crme.2018.11.002.

[12] H. Feng, S. Jiang, & A. Ji (2019). Investigations of the static and dynamic characteristics of water-lubricated hydrodynamic journal bearing considering turbulent, thermohydrodynamic and misaligned effects. *Tribol. Int.*, 130, 245–260. doi: 10.1016/j.triboint.2018.09.007.

[13] D. Milčić, A. Alsammarraie, M. Madić, V. Krstić, & M. Milčić (2021). Predictions of Friction Coefficient in Hydrodynamic Journal Bearing Using Artificial Neural Networks. *Strojniški Vestn. – J. Mech. Eng.*, 67(9), 411–420. doi: 10.5545/sv-jme.2021.7230.

[14] J. Ma, C. Fu, W. Zhu, K. Lu & Y. Yang (2022). Stochastic Analysis of Lubrication in Misaligned Journal Bearings. *J. Tribol.*, 144(8), 1–13. doi: 10.1115/1.4053626.

[15] H. Zhang, X. Lin & S. Jiang (2023). Static Characteristics of High-Speed Water-Lubricated Journal Bearing Considering Turbulence and Cavitation Effects. *J. Tribol.*, 145(12), 1–12. doi: 10.1115/1.4063025.

[16] J. Wang, Sen Jiang, Jiuqi Huang, Wencai Xiong, Jingwei Hu, Zhaozhe Meng, Ange Nsilani Kouediatouka & Guangneng Dong (2023). Simplified Calculation of Recess Pressure Considering the Hydrodynamic Effect. *J. Tribol.*, 145(6), 1–11. doi: 10.1115/1.4056740.

[17] K. J. Stout & W. B. Rowe (1974). Externally pressurized bearings design for manufacture. Part 3 - design of liquid externally pressurized bearings for manufacture including tolerancing procedures. *Tribology*, 7(5), 195–212. doi: 10.1016/0041-2678(74)90118-3.

[18] W. B. Rowe (2021). Conical hydrostatic journal bearings for high speeds. *Proc. Inst. Mech. Eng. Part J J. Eng. Tribol.*, 235(4), 808–819. doi: 10.1177/1350650120929251.

[19] G. Hong, L. Xinmin & C. Shaoqi (2009). Theoretical and Experimental Study on Dynamic Coefficients and Stability for a Hydrostatic/Hydrodynamic Conical Bearing. *J. Tribol.*, 131(4), 1–7. doi: 10.1115/1.3176991.

[20] S. Heller & W. Shapiro (1969). A Numerical Solution for the Incompressible Hybrid Journal Bearing With Cavitation. *J. Lubr. Technol.*, 91(3), 508–515. doi: 10.1115/1.3554973.

[21] M. A. Dumbrava (1983). Mathematical models of externally pressurized hybrid bearings. *Wear*, 84(2), pp. 125–137. doi: 10.1016/0043-1648(83)90259-4.

[22] W. Kalita, C. M. Rodkiewicz & J. S. Kennedy (1986). On the Laminar Flow Characteristics of Conical Bearings. Part I—Analytical Approach. *J. Tribol.*, 108(1), 53–58. doi: 10.1115/1.3261143.

[23] W. Kalita, C. M. Rodkiewicz & J. S. Kennedy (1986). On the Laminar Flow Characteristics of Conical Bearings. Part II—Experimental Verification. *J. Tribol.*, 108(1), 59–64. doi: 10.1115/1.3261143.

[24] Z. Guo, T. Hirano & R. G. Kirk (2005). Application of CFD analysis for rotating machinery - Part I: Hydrodynamic, hydrostatic bearings and squeeze film damper.

J. Eng. Gas Turbines Power, 127(2), 445–451. doi: 10.1115/1.1807415.

[25] E. R. Michael & M. Khonsari; Booser (2017). *Applied Tribology: Bearing Design and Lubrication* (3rd Edition). Wiley.

[26] O. Reynolds (1886). On the Theory of Lubrication and Its Application to Mr. Lowe's Experiments Including an Experimental Determination of the Viscosity of Olive Oil. *Philos. Trans. R. Soc. London*, 177, 157–234.

[27] W. B. Rowe (2012). *Hydrostatic, Aerostatic, and Hybrid Bearing Design* (1st Edition). Butterworth-Heinemann.

[28] "ANSYS FLUENT 12.0 Theory Guide".

[29] Genichi Taguchi, Subir Chowdhury & Yuin Wu (2005). *Taguchi's Quality Engineering Handbook*. Wiley.